

**Stability assessment of forecasts
regarding ice supersaturation and
persistent contrails**

Master's Thesis

at the Faculty of Physics,
Ludwig-Maximilians-University Munich

conducted at the
German Aerospace Center (DLR) in Oberpfaffenhofen
at the Institute of Atmospheric Physics

Supervisor: Prof. Dr. Anja Schmidt

Co-Supervisor: Dr. Klaus Gierens

Co-Supervisor: Dr. Luca Bugliaro

submitted by

Georg von Bonhorst

Munich, 15th Oktober 2024

**Stabilitätsbeurteilung von
Vorhersagen zur Eisübersättigung
und persistenten Kondensstreifen**

Masterarbeit

vorgelegt von

Georg von Bonhorst

ESM Gruppe

Institut für Physik der Atmosphäre

DLR

Betreuer: Prof. Dr. Anja Schmidt

Weiterer Betreuer: Dr. Klaus Gierens

Weiterer Betreuer: Dr. Luca Bugliaro

München, den 15.10.2024

Abstract

In order to achieve the ambitious 2 °C target of the Paris Agreement, it is necessary to reduce the climate effect of all sectors, including aviation. The reduction of non-CO₂ effects, especially through contrail avoidance, seems a quick and relatively easy way to reduce the climate impact of aviation. Several studies have shown that this would be achievable with only a very small increase in fuel consumption on the order of 0.1 %, but these studies assumed that perfect weather forecasts were available for the prediction of contrails and for flight planning which aims at avoiding contrails. Obviously, this is an invalid assumption, as predictions are always subject to errors. It needs to be clarified what this assumption implies for contrail avoidance. Our results show that the quality of the forecast of persistent contrails decreases with increasing temporal gap between flight planning and the actual flight time. During this time, the regions where contrails can form may develop differently in nature than in the forecast model due to non-linear dynamics of the atmosphere. This results in correct forecasts, but also in false alarms and misses. In an example case with a large, yet realistic, time gap on $623 \cdot 10^3$ km planned flight distances persistent contrails were predicted, but occurred actually on $464 \cdot 10^3$ km. Additionally, $135 \cdot 10^3$ km of contrails occurred unexpectedly (misses). The false alarms and misses can spoil the climate benefit of contrail avoidance measures. An analogous mechanism would apply for the prediction of other non-CO₂ effects of aviation. Several ways to improve the contrail forecast are conceivable. In particular, assimilation of relevant data, such as relative humidity in the upper troposphere, would help to keep the forecast model close to reality. A better representation of ice supersaturation (relative humidity w.r.t. ice over 100 %) in the models seems necessary as well. Meanwhile, considering the most recent available weather forecast could already help to minimise false alarms and misses.

Contents

1	Introduction	1
2	Theoretical background on contrail formation and persistence and their radiative effects	7
2.1	Relative humidity, saturation and supersaturation	7
2.2	Aircraft plumes, their composition and evolution	9
2.3	Contrail formation: the Schmidt-Appleman Criterion	10
2.4	Contrail persistence: Ice supersaturation	12
2.5	Contrail radiative effect	13
3	Data and Methods	15
3.1	Weather-data	16
3.1.1	Cloud schemes	17
3.2	Methods	18
3.2.1	Pearson-correlation	18
3.2.2	Comparison of forecast fields	19
3.2.3	Flight-trajectories	20
3.2.4	Scores	20
3.2.5	Maximum random overlap	21
3.3	Experiments conducted	22
4	Results and Discussion	25
4.1	Ensemble vs. deterministic forecasts of potential contrail cover	25
4.2	Strategic contrail avoidance under imperfect weather forecast	32

4.2.1	Results	32
4.2.2	Discussion	41
5	Conclusion and Outlook	45
	Bibliography	51
	Acknowledgements	65

Chapter 1

Introduction

Global warming is not just an abstract danger, but a real threat. Today we already see frequent severe weather events, such as flooding, droughts, and hail. In addition to acute symptoms, there are also slower ones, such as the increase in sea level [18], the change in ocean circulation [80], oxygen depletion [35, 40] or ocean acidification [59, 42, 94]. All these environmental threats led to multiple agreements. One of them is the famous Paris agreement, supported by most countries in the world. The goal is to keep the average surface warming, and therefore stop climate change, below 2.0 °C, if possible below 1.5 °C. [50] This threshold was chosen because scientists expect the changes, partly irreversible, to our ecosystem to be manageable with relatively low effort under this condition.

To reach this ambitious goal, not only the large sectors of heating and industry need to reduce their impact on the climate (reduction of CO₂ emissions, reduce, reuse, and recycle resources) but also the transportation sector. [83] In the transportation sector, actions to reach the climate goal are to increase efficiency, to change propulsion concepts to environmentally friendlier ones, or to use other smart methods to reduce the impact on climate. All sections of transportation need to reduce their impact on climate, including aviation. Aviation has some special characteristics with respect to its climate impact, since next to CO₂ effects there are also a number of significant non-CO₂ effects. Although the number of vehicles is comparably low, aviation still has 3.5% of the total anthropogenic climate forcing - a substantial impact on the environment. [44]

For aircraft, most technical measures would need a long time for development, testing and implementation. They are quite expensive and aircraft with current technology will still be in use for many years. Furthermore, gaining efficiency is quite difficult, as the propulsion systems are already highly optimised. Switching the propulsion system is also by no means an easy task due to strict space and

weight constraints. Even though there are already prototypes for short-range electric aeroplanes [10] and first concepts of hydrogen aircraft, more technical development is required until they are fit for mass production. The use of sustainable aviation fuel (SAF) is another possibility to get one step closer to sustainable aviation. Although the technical transition of aircraft to the new fuel is possible, the production and supply is nowhere near sufficient for all air traffic. [26, 17]

A different concept to decrease the climate impact of aircraft would be the transfer to other more efficient transport methods such as ships or trains. This is certainly an option, but aircraft offer the benefit of speed, comparatively low infrastructure expenses, and are sometimes indispensable for certain purposes.

However, there are still more options to reduce climate impact of aviation, such as intermediate stop operation or flying in formation. The former option leverages the reduced take-off weight by carrying less surplus fuel, leading to fuel savings of up to 9% for a global fleet. However, this comes with the disadvantage of prolonged flight durations due to the need for intermediate stops. [43] The benefit of the latter option of flying in formation is that a trailing aircraft can surf on the wake vortex created by the leading aircraft. The updraft generated by the wake vortex produces lift for the trailing aircraft leading to fuel savings of up to 9%. [89, 86, 41] (These energy savings are also one reason why geese fly in V-formation.)

A peculiarity of aviation is that it has quite large non-CO₂ effects. Therefore, reduction of non-CO₂ effects is another possibility to reduce the climate impact of aviation. Those non-CO₂ effects originate from the emission of NO_x, SO_x, water vapour, particular matter, soot, lubrication oil [82] and contrail formation. Non-CO₂ climate effects are of the same order as CO₂ climate effects or even larger.[44] However, for a single flight the non-CO₂ effects depend heavily on the emission position, synoptic weather situation, and other properties of the surrounding atmosphere due to the relatively short lifetime of the individual effects. Determining the precise magnitude of non-CO₂ components is challenging due to significant variability with synoptic conditions, selected timescale/metric, specific location and timing.

In a paper from Lee et al. [44] the non-CO₂ effective radiate forcings (ERF), a way to assess the climate impact, are estimated to have roughly 2/3 of the total ERF from aviation (0.1 W/m²). However, the uncertainties of the non-CO₂ ERF are a factor of eight larger than the uncertainties of CO₂ ERF. The largest part of non-CO₂ ERF is due to persistent contrails. Therefore, it is desirable to reduce or avoid contrail formation. The radiative effect of contrails works like that of a natural cirrus cloud. Short-wave radiation from the sun is partly reflected to space and therefore is not available as heat for the earth system. Long-wave radiation is effectively re-emitted back to Earth. [66, 91] The contrails are colder than the earth surface, making it look

from space as if the earth were colder. Since blackbody radiation flux is coupled to temperature via the Stefan-Boltzmann law ($\propto T^4$), the outgoing long-wave radiation is reduced. The total effect of contrails is the combined effect of the short-wave and the long-wave effect. Apart from the position of the sun, there are numerous factors such as synoptic weather situation [90], crystal size, and relative humidity that influence the effective radiative forcing of a contrail.[51] For an estimation of the climate impact of contrails it is necessary to run climate models over a longer period of time, such as in Burkhardt et al. [9] or Gettelman and Chen [22]. [8, 6] In the global average over at least a year, contrails seem to be warming [74]. If we want to reduce the climate impact of contrails, we must avoid contrails that warm the most. For a single contrail and the decision whether it should be avoided or not, running a climate model is not possible. Hence, approximations such as CoCiP (Contrail Cirrus Prediction model) [66] or ACCF (Algorithmic Climate Change Function) [93] have been invented to quickly calculate the first approximation of the climate effect. The speed is critical for operational use.

An advantage of contrail avoidance compared to the mitigation of other non-CO₂ effects is that contrail formation can be observed and therefore verified via ground-bound cameras [47] and satellite images [20, 46].

There are several ways summarised in Noppel and Singh [54] and Gierens [29], how the formation of contrails can be prevented and thus their radiative forcing reduced. Not all of them are feasible or desirable, as they partly lead to suboptimal technical modifications. An attempt is to introduce substances such as alcohols to inhibit contrail formation. [69] However, this method is not ideal, as it introduces other adverse atmospheric effects. [29] But there are also usable approaches such as the following:

Alternative Propulsion Systems One way to reduce contrail formation is to switch to new propulsion concepts that either have no water vapour emissions at all (battery powered aircraft), lower water emissions (Water-Enhanced Turbofan, WET [56, 63]) or lower condensation particle emissions (e.g. lean combustion [87]). In addition to reducing contrails, these propulsion concepts also have increased efficiency, which reduces the energy consumption of an aircraft. However, aircraft manufacturers need many years to build and test a new propulsion concept. It is therefore not possible to rely on this option in the near future.

Particle Reduction Alternatively, the number of particles emitted can be reduced by new propulsion concepts or new fuels such as SAF. The reduction of particles, such as soot, leads under certain conditions to the formation of fewer ice

crystals. This in turn reduces the optical thickness and shortens the lifetime of the individual contrails. The lifetime is shorter because, with the same available moisture, the reduced number of nuclei leads to the growth of larger ice crystals, which sediment more quickly due to their size. Both the reduced optical thickness and the shortened lifetime reduce the ERF of the contrails. [29, 38, 49] But this helps only up to a certain point, as research by Bier et al. [7] demonstrated that contrails can form even without soot or particle emissions due to the crystallisation nuclei already present in the air.

Diverting Flights The first two options dealt with the technical possibilities on the aircraft itself. However, the properties of the atmosphere also play a significant role in the formation and effective radiative forcing of contrails in addition to the properties of the aircraft. This is another lever to avoid contrails. There are several ways to do this, which are explained in turn in the following paragraphs. The approaches can be roughly divided into Changing the flight times, globally changing the flight altitude, and diverting depending on the situation. Theoretically, these options could be implemented immediately in air traffic without requiring changes to the aircraft. Nevertheless, since air traffic has tight security requirements, new procedures and rules have to be developed by the air traffic control, airlines and lawmakers. This should be achievable within a relatively short time frame, at least in comparison to revolutionary technical development.

Changing the flight times would exploit the variation in radiative forcing due to the zenith angle of the sun. Since the long-wave effect hardly changes throughout the day, the total radiation effect is mainly dependent on the short-wave effect. This option would require concentrating flights during the morning and evening, when the cooling effect is maximised. [53, 74]

The change in flight altitude attempts to divert flights into regions of the atmosphere where persistent contrails rarely form. By going up to higher altitudes in the extratropics, one would reach the stratosphere. The stratosphere is so dry that the contrails evaporate quickly in the surrounding air. This reduces persistent contrails but also leads to the introduction of water into the dry stratosphere. The water has a high lifetime there and therefore a strong climate impact.[55] The other possibility is to lower the altitude of air traffic such that the ambient air is warm enough to inhibit contrail formation. However, this option would force aircraft to non-optimal altitudes with higher drag and turbulence, thus increasing fuel consumption and emissions. Several studies have investigated vertical rerouting [60, 14], but as Teoh et al. [78] showed, most altitude change strategies are suboptimal and situational rerouting appears to be favourable.

The possibility of contrail avoidance by diverting flights is being investigated in the LuFO VI D-KULT project, to which this Master's thesis also belongs. The idea behind this is to avoid regions in which contrails persist or grow for a longer period of time due to sufficient moisture. These regions are also known as ice-supersaturated regions (ISSR). [28] Another condition is that contrails are formed at all: This can be calculated using the Schmidt-Appleman Criterion. [64, 65] These condition is elucidated in Chapter 2. There are at least two ways to avoid the ISSR.

First, the blocking of airspaces in which contrails can occur for all aircraft as in Sausen et al. [61]. Another approach is the vertical and horizontal rerouting of individual flights through tactical (inflight) and strategic (preflight) measures. This has the advantage that airspace is not completely blocked. However, individual rerouting does not guarantee that no other aircraft in this region will generate a contrail and that rerouting other aircraft would therefore be in vain. The closure of airspace generally leads to capacity restrictions

According to Frias et al. [15], it is possible to avoid a large part of the non-CO₂ effect of contrails (73.0%) with only a small increase in fuel consumption (0.11%). These results are promising and motivate us to continue with this approach. However, the cited study unrealistically assumed that the weather forecast used corresponds to the "true" weather. This assumption may lead to overoptimistic results and may trigger unrealistic expectations. Therefore, the present thesis analyses the influence of the imperfect weather forecast on contrail avoidance. More specifically, this thesis attempts to determine how the forecast of areas where contrails can persistently develop evolves for longer forecast horizons. Implicitly, the aim is to understand how far the forecast differs from the true weather depending on the forecast horizon and what this implies for rerouting.

The Master's thesis is structured as follows: Chapter 2 elucidates the physics of the formation of contrails and the corresponding atmospheric conditions. In the next chapter 3, the data and methods used are presented in more detail. In chapter 4, the results of our analysis are shown and discussed. The final chapter 5 summarises the findings of this work and outlines further steps.

Parts of this Master's thesis are already submitted in the paper von Bonhorst et al. [88]. This paper was written in collaboration with the authors Moritz Maizet and Klaus Gierens. Moritz Maizet has contributed figures 4.9, 4.10, 4.12 and 4.13. Klaus Gierens discussed and helped me with the content and text.

Chapter 2

Theoretical background on contrail formation and persistence and their radiative effects

This chapter presents the theoretical background for persistent contrails. In the first part, the notions relative humidity, saturation and supersaturation are explained. In the next remaining parts, we give an account of contrails, their evolution, their persistence and their radiative effects. Most of the statements, unless otherwise specified, are taken from Gierens [29] and Gierens et al. [28].

2.1 Relative humidity, saturation and supersaturation

Contrails are ice clouds created by aircraft and behave similarly to their natural counterpart, the natural cirrus. Clouds in general consist of water in the form of liquid droplets or solid ice crystals floating in the air. Cirrus clouds are ice clouds and, therefore, consist mainly of ice crystals, which is also the reason why they only form at low temperatures.

The water molecules in a cloud are incessantly in exchange between the gaseous phase (water vapour) and the liquid phase (liquid droplets) or solid phase (ice crystals). This is shown in figure 2.1. As soon as the fluxes between two phases equalise, this is referred to as dynamic equilibrium. In relation to water vapour, this is also called saturation. Saturation can occur in relation to one of the two phases of water. For exchange with liquid droplets it is called liquid saturation, and for exchange with ice it is called ice saturation. The vapour pressure at liquid saturation is larger

than that at ice saturation. Both saturation pressures depend primarily almost exponentially on the temperature, as postulated by the Clausius-Clapeyron equation. It can be assumed that the specific volume of the condensed phase is negligible. In this case the Clausius-Clapeyron equation takes the following form:

$$\frac{d \ln e}{dT} = \frac{L}{RT^2} \quad (2.1)$$

Here L is the latent heat for the corresponding phase transition (phase transition between water vapour and ice or water) and R is the special gas constant for water. With the assumption that L is independent of the temperature T , equation 2.1 can be integrated:

$$e(T) = e(T_0) \exp\left\{ \frac{L}{RT_0} \frac{T - T_0}{T} \right\} \quad (2.2)$$

Actually, L is weakly temperature dependent, which leads to slight deviations from equation 2.2. The true water vapour saturation function has therefore approximated by several authors, both for water vapour saturation pressure with respect to (w.r.t.) water or ice. [36, 52, 45, 79, 70]

Since water vapour pressure in the atmosphere covers several orders of magnitude and no statement can be made about the physical state based on its value, it makes sense to convert the humidity into a percentage value (relative humidity) in relation to a reference value. In detail, relative humidity is defined as the ratio between the actual water vapour pressure and the reference pressure, which are the two saturation pressures. Therefore, there are two kinds of relative humidity: RH (relative humidity w.r.t. liquid water) and RH_i (relative humidity w.r.t. ice). The new variables have the advantage, that they mostly lie between 0–100% and are better at describing the physical processes such as condensation or nucleation.

Nevertheless, nothing prevents the vapour to obtain higher pressure than saturation pressure in clear air. This is called supersaturation. Supersaturation is needed to initiate the formation of droplets or ice crystals, the so called nucleation.

In contrail formation (see below), first liquid droplets are nucleated which requires liquid supersaturation. These droplets freeze in sufficiently cold air and the formed ice crystals need ice (super)-saturation in order to persist for longer than just a few seconds or minutes.

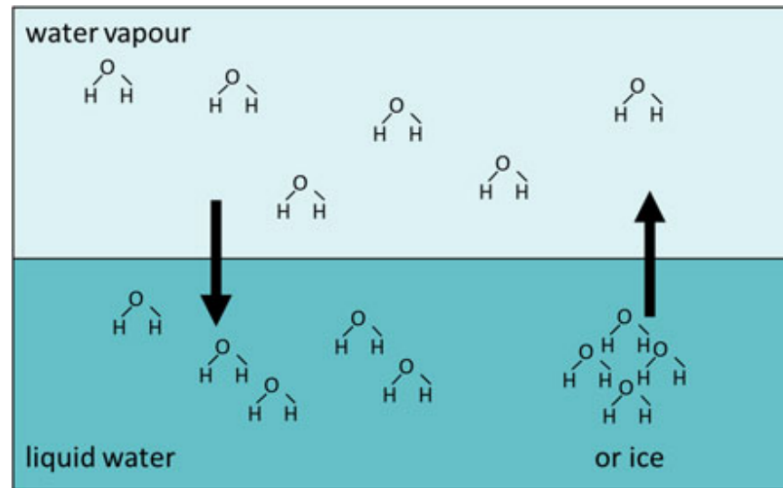


Figure 2.1 This figure visualises the thermodynamic way of thinking about an interface between two phases of a material. The gaseous phase of water is shown in light blue. The dark blue colour shows either the liquid phase (water) or the solid phase (ice). The black arrows are the flows of water molecules between the two phases. If the two arrows are the same size, the two phases are in what is known as dynamic equilibrium. The illustration was taken from the chapter "Ice supersaturation" by Gierens, Spichtinger, and Schumann [28].

2.2 Aircraft plumes, their composition and evolution

Persistent contrails are contrails that last at least longer than about 10 min. The formation of contrails is connected to the evolution of the exhaust plume. Over its lifetime, the plume can be roughly divided into the jet-, vortex-phase and the diffusion regime.

The first phase, the jet phase, lasts for about 10 s. In this phase, the plume is driven by the dynamics of the engine exhaust. The several hundred degree hot exhaust plume additionally typically consists of approximately 1.25 kg water [65, 64] and in the order of 10^{15} soot particles and 10^{17} non-volatile particles [38] per kg fuel burned compared to ambient air. (These values heavily depend on the propulsion system and the fuel, the values here are an estimation for aircraft that burn kerosene. There are also other emissions, but they do not play a role in the formation of contrails.) The exhaust gas quickly cools during the first phase by entrainment of the surrounding air, the plume is hereby expanded in an isobaric way. The plume cools from 500-600 K to almost ambient air temperature. [21] If water vapour saturation w.r.t. water is reached during this cooling process, contrails will form after approximately 1/3 of a second. The criterion for the formation of a contrail is called the Schmidt-Appleman criterion and will be explained in more detail later.

In the second phase, the vortex phase, the plume is affected by the so-called wing-tip-vortices. These two inward counterrotating vortices isolate the plume from the surrounding air and let the plume descend several hundred meters. [66, 37, 16] The wing-tip-vortices are created by the generation of lift. [1] During this phase, secondary vortices can be created which stay at flight altitude, this can be seen as secondary contrails over the main plume. [75] The secondary vortex contains roughly between 10–30% of the plume. [21] The vortex phase that lasts up to around 300 s during which the temperature rises only due to adiabatic compression of the air in the sinking vortex. The rise of temperature can lead to the evaporation of newly formed ice crystals. Due to the temperature increase the plume can rise again in stably stratified atmosphere back to the emission level. [30, 85, 84]

After the vortices dissipate, the final phase begins. In this phase, the plume with the freshly formed contrail comes into contact with the environment and diffuses into it. Whether the contrail dissipates quickly or survives for a longer time depends on the atmospheric conditions of the environment. Ice supersaturation is necessary to prevent the crystals in the contrail from evaporating. This phase can last several hours.

2.3 Contrail formation: the Schmidt-Appleman Criterion

For the creation of contrails, ice crystals have to be nucleated. However, the soot particles in the exhaust plume are unsuitable as ice nuclei. The formation of ice crystals proceeds via the liquid phase. [39] That means that first droplets form (mainly) on the soot particles which freeze in sufficiently cold air. This implies that the expanding plume must transiently attain liquid supersaturation. This is the central point of the Schmidt-Appleman Criterion (SAC). It is convenient to view the isobaric mixing process in a Temperature vs. water vapour partial pressure phase diagram.

In Figure 2.2 this is sketched. The two dotted lines show two mixing lines which are straight because the mixing is isobaric. The left solid line represents the saturation vapour pressure with respect to liquid water whereas the right one represents the saturation with respect to ice. The mixing line which is tangent to liquid saturation curve, represents a case where a weak contrail would just form. Contrails do not form if the mixing line would be located to the right of this threshold mixing line. The other mixing line on the left to the threshold line leads through liquid supersaturated conditions which means that a contrail forms.

Whether a contrail forms or not depends inter alia on the slope of the mixing line, G , which is defined by:

$$G = \frac{\Delta e}{\Delta T} \quad (2.3)$$

Δe is hereby the change in water vapor partial pressure in the expanding plume and ΔT the corresponding temperature change.

With the help of equation 2.4 one can find the temperature T_M where the slope of the water vapour saturation curve has the value G . [64] This is also the maximum temperature at which a contrail can be formed.

$$T_M = -46.46 + 9.43 \ln(G - 0.053) + 0.720 [\ln(G - 0.053)]^2 \quad (2.4)$$

Since the mixing trajectory is a straight line in Phase diagram with the slope G , it is simple to calculate for given atmospheric temperature and water vapour pressure whether a contrail can form or not. If the relative humidity is given, a maximum temperature which allows contrail formation can be computed with the following equation:

$$T_C = T_M - \frac{e_{sat}(T_M) - U e_{sat}(T_C)}{G} \quad (2.5)$$

$U = \frac{e}{e_{sat}}$ is hereby the relative humidity. If however the ambient temperature T_C is given, one can deduce a minimum water vapour pressure that is necessary for contrail formation.

$$e_{crit} = e(T_M) - (T_M - T_C) G \quad (2.6)$$

For practical purposes, it is important to express the slope G in terms well known properties of the fuel, aircraft and ambient conditions. For kerosene driven aircraft Schumann has derived the following equation, exploiting conservation laws for mass, momentum and energy. This is known as the Schmidt-Appleman Criterion.[64, 65, 62, 2]

$$G = \frac{EI_{H_2O} p c_P}{\epsilon Q(1 - \eta)} \quad (2.7)$$

EI_{H_2O} is the water vapour emission index, which for kerosene burning is typically 1.25 kg water per kg fuel. Q is the combustion heat of fuel, which is about 43 MJ/kg. η is the overall propulsion efficiency (0.3–0.4 are typical values). It is included in the equation since only a fraction of ηQ of the chemical energy is used to propel the aircraft, the remaining part heats the exhaust gases. p is the ambient pressure and c_p is the specific heat capacity of the air at constant pressure. $\epsilon = 0.622$ is the

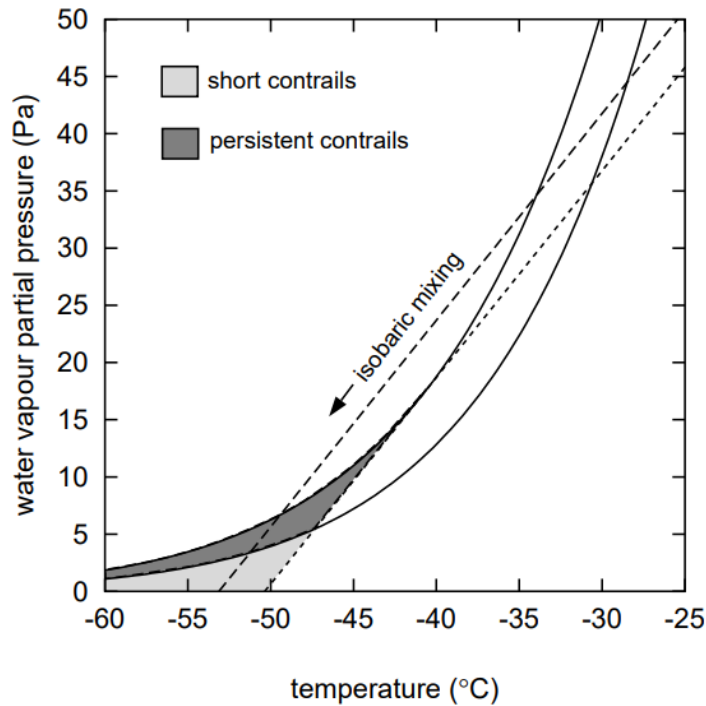


Figure 2.2 T-e phase diagram of contrail formation. The two solid lines are the saturation vapour pressure curves (the upper one with respect to water and the lower one with respect to ice) as a function of temperature. The two dashed lines with the same gradient show possible isobaric mixing curves of hot moist exhaust gases and cold dry ambient air. If the straight lines intersect the vapour pressure curve w.r.t. water (left straight line) or are at least tangent to it (right straight line), condensation trails can form. If the air mixture remains in the dark grey area, the contrail can persist for a long time or even grow. In the light grey area, on the other hand, the contrail only remains for a short time and the ice crystals in the contrail sublime into the surrounding air. The illustration is from the chapter "Contrails and Contrail Cirrus" by Gierens [29]

ratio of molar masses of water and air. For current kerosene propelled aircraft G is typically of the order 2 Pa/K. Note that the formula for the G-factor is different for other propulsion. [92, 23]

2.4 Contrail persistence: Ice supersaturation

The SAC tells us only if a contrail is formed or not. Whether it is persistent, that is whether its ice crystals will survive for longer than a few seconds to minutes, depends on the ambient RH_i . The ambient air should be supersaturated with respect to ice. This prevents the ice crystals inside a contrail to evaporate. Furthermore, this is also the condition for the ice crystals to grow. That is, in an ice-supersaturated region, contrails can grow. In Figure 2.2 the dark grey shaded area depicts the conditions for a contrail to be permanent. However, the conditions represented by the light grey shaded area let the ice crystals evaporate, leading to the disappearance of the

contrail within a short time.

Theoretically, contrails would also grow when the water vapour is supersaturated w.r.t. water. However, since clouds form spontaneously under these conditions which would immediately freeze to form cirrus, the climatic effect of contrails would be negligible here.

Areas in which the supersaturation occurs w.r.t. ice, but not to water, and where no clouds have formed yet are therefore of particular interest. We call these areas ice supersaturated region (ISSR). The ISSRs are typically several hundred metres high. [81, 57, 11] The horizontal extent of ISSRs has been estimated from flight path lengths (MOZAIC project [48]) through ice-supersaturated airmasses which results in about $150 \text{ km} \pm 250 \text{ km}$. [24] The large standard deviation is due rare cases where the flight path through an ISSR was more than 1000 km. On average about 15% of flight paths on cruise altitude occur in ISSRs. [25] ISSRs are therefore not uncommon in the atmosphere. [28] The exact heights of the ISSRs vary depending on latitude. Due to the warmer atmosphere in the tropics, the ISSRs there are higher at 140 hPa than at mid-latitudes around 200-250 hPa. In general, with a few exceptions such as the Antarctic, the ISSRs lie below the tropopause in the upper troposphere. [71]

ISSRs usually form where the air rises and, therefore, cools. This is the case over large areas in the tropics in the so-called tropical transition layer or along storm tracks in the mid-latitudes. Depending on whether the air lift is large-scale or localised, the lifespan can range from a few hours to around a day. [73, 72, 4] However, care must be taken here, as ISSR is not an inherent quantity of the air mass such as absolute humidity, but only a state. The ISSR do not necessarily follow the movement of the winds.

2.5 Contrail radiative effect

The climatic effect of contrails and the resulting cirrus clouds follows the same principles. There are two opposing effects, one cooling and one warming. The total climatic effect is the sum of the two.

The warming effect results from the reduction of long-wave radiation emitted into space due to contrails. Contrails absorb the long-wave radiation from below (e.g. from the earth surface) and emit less long-wave radiation further than they absorbed from below. The difference in radiation comes from the temperature difference between the cold, high contrail cirrus clouds and the warmer earth surface or lower clouds. Since thermal radiation follows the Stefan-Boltzmann law, which is proportional to T^4 , even small temperature differences lead to considerable differences in

long-wave radiation. With contrails, the Earth looks locally from space like a colder body.

The cooling effect is caused by contrails reflecting short-wave light coming from the Sun back to space. This effect depends strongly on the angle of incidence of the light and, therefore, on the position of the Sun. The cooling effect is not present at night and is strongest when the sun is low in the sky. [53]

The total radiative effect of a contrail is therefore dependent on the position of the Sun, the optical thickness, the extension of the contrail, the lifetime, and the surroundings. [51, 66, 91, 76] For example, contrails are always warming at night but may or may not cool during the day. [74] The individual radiative effect of a single contrail can range from several -10 W/m^2 up to several $+10 \text{ W/m}^2$. The distribution of the individual effect peaks at a few W/m^2 in the positive part of the PDF (warming) and has an approximately exponential decay toward higher values. The mean value is positive as well. [90]

The radiation effect of contrails is significantly reduced if there are cirrus clouds or other contrails in the vicinity. It can also happen that contrails deprive other contrails of the available water in the atmosphere, and hence of the possibility to grow. This modifies the radiation effect of the contrail considered.

In order to determine the climate effect of contrails it is necessary to run climate models over a long time period, as in Burkhardt et al. [9]. [8, 6] On a global annual average, contrails are warming.

Chapter 3

Data and Methods

As the goal of this thesis is to analyse the impact of an imperfect weatherforecast on avoiding contrails, we undertake to study the differences of the weather forecast at a time of flight planning to the real weather at the time of the flight. As the real weather is not at hand we use the most recent forecast as a proxy for reality. This chapter first describes the weather data used. Then we introduce the mathematical methods that we use for comparison. These include the correlation of fields from two different forecasts and its dependence on the temporal distance between the forecasts. Furthermore, we evaluate such fields in terms of correct positives (i.e. contrail forecasted and confirmed), correct negatives (contrails not forecasted and not confirmed), false alarms (contrail forecasted but not confirmed), and misses (contrail not forecasted but confirmed). For a simple illustration, we also use artificial flight paths and consider where the four categories of the comparison are met along the flights. These events are analysed with a contingency table and two scores, the critical success index and the equitable threat score. As we are also interested in the cloudiness that is ambient to predicted contrails, we further investigate the high-altitude cloudiness, to which we employ the maximum random overlap method to determine the effective local coverage. Finally, a description of the experimental procedure is provided.

Note that the data used and a part of the methods have been applied already for the mentioned paper [88]. The corresponding sections, written in collaboration with Klaus Gierens, have been slightly adapted for this thesis, but they have not been completely reformulated. The text from sections 3.2.1, 3.1.1 and 3.2.5 is not taken from the paper.

3.1 Weather-data

This study is based on special aviation weather forecast data provided by the German Weather Service (DWD) within the German LuFo-VI-2 project D-KULT (Demonstrator Klima- und Umweltfreundlicher Lufttransport; Demonstration of climate- and environmentally friendly air transport), funded by the Federal Ministry for Economic Affairs and Climate Action. DWD issues four times per day the WAWFOR (World Aviation Weather FORcast) data packages that are derived from the regular weather forecast produced with the ICON model. WAWFOR is available globally (spatial resolution $0.125^\circ \times 0.125^\circ$ in longitude and latitude) and, with higher spatial resolution, for the European region (EU nest: $23.5^\circ\text{W} - 62.5^\circ\text{E}$, $29.5^\circ\text{N} - 70.5^\circ\text{N}$, resolution $0.0625^\circ \times 0.0625^\circ$, approx. $6.5\text{ km} \times 6.5\text{ km}$); we use both. For D-KULT, WAWFOR is enriched with additional data sets, WAWFOR-Klima-X, where the "X" stands for further specifications. Here we use the WAWFOR package 1 (EU-nest, global), WAWFOR-Klima-1 (EU-nest, global), and WAWFOR-Klima-1s (global). While Klima-1 includes output from the operational one-moment microphysics scheme, Klima-1s uses experimental runs of ICON equipped with a two-moment scheme based on the work of Seifert et al. [68]. These data sets contain in particular the following fields:

PPC: potential of persistent contrails — a binary value (0/1), with $PPC = 1$ indicating a grid box where persistent contrails are possible;

PPC_prob: fraction of ensemble forecast members that have $PPC = 1$ — a real number between 0 and 1.

CLC: cloud coverage fraction — Percentage (0 – 100), where $CLC = x$ means that x percent of a grid box is cloudy and $(100-x)\%$ are clear.

The exact calculation procedure of the variables varies slightly depending on the specific data set. *PPC* is computed using temperature and relative humidity from the regular forecast, applying the Schmidt-Appleman criterion [64] with an overall propulsion efficiency of $\eta = 0.365$. The criterion of ice (super)saturation is assumed for values of relative humidity with respect to ice (*RHi*) that exceed 93%, in order to balance a low humidity bias in the forecast [31], for the Klima-1 data (EU-nest, global). For the EU-nest of the WAWFOR-Klima-1 data set, there is an additional variable *PPC_prob*, which is intended to reflect the uncertainty of the forecast. Instead of a deterministic run for *PPC*, 40 ensemble members with simplified physics and slightly different initial conditions are used. PPC_{prob} is basically the number of members of the 40-member forecast ensemble that predict $PPC = 1$, divided by the total number of ensemble members (40); It can thus obtain values $n/40$; $n \in \mathbb{N}_0, 0 \leq n \leq 40$. This gives us a probability instead of a binary value.

A similar idea is behind the *PPC* calculation for the experimental data set WAWFOR-Klima-1s. Whereas WAWFOR-Klima-1 (EU-nest, global) uses the output of a deterministic run, the WAWFOR-Klima-1s (global) takes the average of 10 ensemble runs. For this experiment, no deterministic run is performed. To compute *PPC* in the ensemble mean, *RHi* is averaged at all grid-points where the Schmidt-Appleman criterion is fulfilled. If this average equals or exceeds 100%, $PPC = 1$ is output, otherwise and at all other grid-points $PPC = 0$. Regarding the threshold value for ice supersaturation a tuning is deemed not necessary for the two-moment scheme. Thus, for the Klima-1s data, ice supersaturation is assumed for $RHi \geq 100\%$. The reason for this is explained in section 3.1.1. A further detail regarding the calculation of the experimental runs with the 2-moment scheme is that they are initialised with the analysis data from the operational ICON run. Thus, the experiment needs a spinup-time of about 6 hours to build up the full ice-supersaturation.

We use cloud fraction (*CLC*) for pressure levels $p \leq 400$ hPa (upper troposphere) in order to estimate (in a crude way) whether the predicted contrails have natural high clouds in their neighbourhood that would diminish their long-wave effect, thereby the warming impact that aircraft rerouting aims to mitigate or prevent.

3.1.1 Cloud schemes

Instead of presenting a full description of the cloud microphysics used in the DWD's ICON model used here in detail, which is outside the scope of this work, we refer to the work of Seifert and colleagues [67, 68] for the two-moment scheme and for the one-moment scheme to the Cosmo documentation [13]. In this section, only the effects on ice supersaturation in the model that are important for this work are discussed.

The one-moment scheme is the operational scheme of cloud microphysics at the time of the Master's thesis. Due to some simplifications, the scheme is fast and efficient, an important factor for time-critical NWP. One of these simplifications is the fact that condensation nuclei for ice (mainly ice crystals) are not a prognostic variable in the model but are parameterised. This parameterisation cannot account for the age of a cloud and thus assumes a large number concentrations of ice crystals already upon first nucleation, which leads to short relaxation times. As a result, ice supersaturation is consumed very quickly down to saturation, and therefore there is insufficient ice supersaturation in the model. One trick to compensate for this is to set the threshold value for ice supersaturation lower than 100% for subsequent calculations such as in Hofer et al. [31].

The two-moment scheme solves this problem by calculating, among others, a pre-

dictive value for the number of ice crystals. As a result, there are fewer ice crystals when a parcel of air becomes supersaturated w.r.t. ice. This leads to longer relaxation times to saturation and thus also to ice supersaturation distributions that are more realistic. In this model version, ice supersaturation is a frequent condition in the upper troposphere, as observed.

3.2 Methods

In the next section, we take a look at the various methods used in this thesis. First, we look at several ways to compare two forecast fields. Scores are used to reduce the results of the comparisons to single numbers. Finally, the maximum random overlap method is presented, which is used to calculate the effective cloud cover.

3.2.1 Pearson-correlation

Correlations can be used to compare two fields and to quantify their similarity. There are various ways to do this, but in this work the so-called Pearson correlation is used. Let X be a forecast field of a variable from the model run m and Y another forecastfield of another variable from the model run n , then we can calculate statistical measures with formulas 3.1. It is necessary that both field have the same coordinate system. The values at certain gridboxes are denoted with small letter.

$$Corr(X, Y) = \sum_{lat} \sum_{lon} \sum_{plevel} \frac{(\bar{X} - x)(\bar{Y} - y)}{\sigma_x \sigma_y} \quad (3.1a)$$

$$N = \sum_{lat} \sum_{lon} \sum_{plevel} 1 \quad (3.1b)$$

$$\bar{X} = \frac{1}{N} \sum_{lat} \sum_{lon} \sum_{plevel} x \quad (3.1c)$$

$$\sigma_X = \sqrt{\frac{1}{N-1} \sum_{lat} \sum_{lon} \sum_{plevel} (\bar{X} - x)^2} \quad (3.1d)$$

Here is $Corr(X, Y)$ the Pearson correlation, N the number of grid points, \bar{X} the mean value of the variable X over all grid points and σ_x the standard deviation.

The Pearson correlation compares the direction of the deviations of two variables from their mean value. However, the correlation only "recognises" linear relationships. The correlation values can lie between -1 and 1 due to normalisation by the two standard deviations.

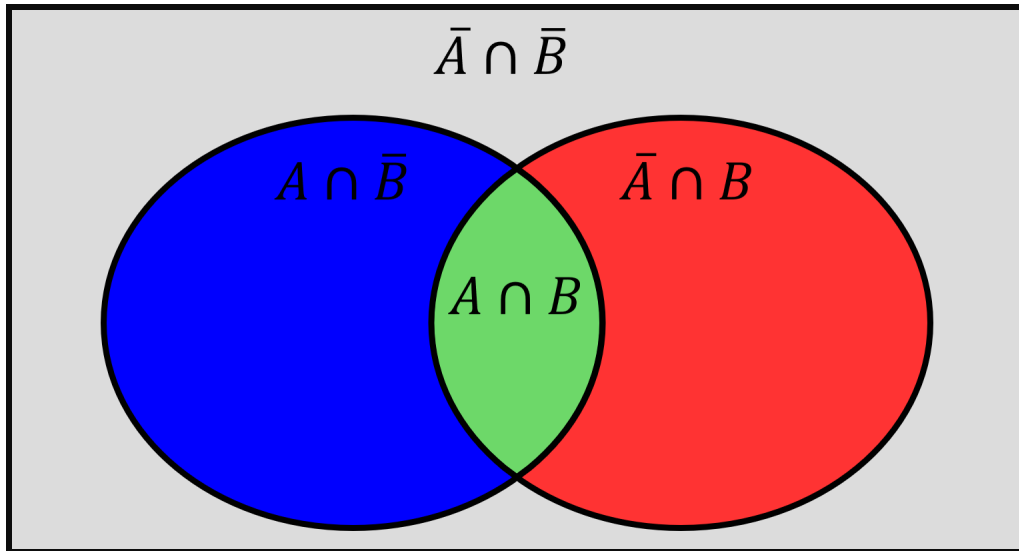


Figure 3.1 Sketch of a Venn diagram with two sets A and B . These two sets represent two PPC forecasts with the same valid time, but a longer (A stands hereby for all gridpoints with $PPC = 1$) and a shorter (B also stands for gridpoints with $PPC = 1$) lead time. The intersection $A \cap B$ is called correct positive, $\bar{A} \cap \bar{B}$ correct negative, $A \cap \bar{B}$ false alarms and $\bar{A} \cap B$ misses. The colour-coding for this diagram is used in other figures throughout this thesis.

A correlation of one means that the deviations of the variable X behave in the same way as the deviations of variable Y apart from a constant prefactor. For -1, the two deviations develop in opposite directions. The two variables are described as uncorrelated if the Pearson correlation is close to 0. This means that it is not possible to draw conclusions about the deviations of the one variable from the deviations of other.

If X and Y are different variables, such correlations are also called cross-correlations. Autocorrelation is a special case of cross-correlation in which X and Y are the same variable but may have a time offset, for example. The latter is used in this study to see how the field similarity evolves with increasing lead time differences.

3.2.2 Comparison of forecast fields

As the two forecasts with different lead times but same valid time share the same grid points, the most direct method to compare them is a point-wise comparison. This allows directly find, mark, and count grid-points for correct forecasts (yes and no), false alarms and misses. All grid-points are covered in this kind of comparison. The corresponding maps can be interpreted as Venn diagrams like in figure 3.1 displaying two sets, A and B : The first set, A , is the collection of grid-points that have $PPC = 1$ in the forecast with the longer lead time. The second set, B , is the analogue, but for the forecast with shorter lead time, a proxy for reality. Furthermore, there is

the intersection of these two sets ($A \cap B$), where both forecasts show $PPC = 1$, and all the remaining grid-points, where both forecasts show $PPC = 0$ ($\bar{A} \cap \bar{B}$). The two sets differences represent false alarms ($A \cap \bar{B}$) and misses ($\bar{A} \cap B$), respectively. The colours in the cross sections in the next Chapter 4 have the same meaning as in the Venn diagram in figure 3.1. The counting of the corresponding grid boxes allows the quantitative evaluation of the forecast skill, see section 3.2.4.

3.2.3 Flight-trajectories

Although the counting of grid boxes that belong to different sets is the easiest way to analyse, it lacks clarity of what this means for flight route planning. The following method is used with the goal to evaluate the impact of the changes within a forecast to potential mitigation measures. There are two possibilities. Either real flight trajectories or artificial ones can be utilised. Real flight trajectories imply one or more case studies, while artificial flight trajectories imply a principal study based on statistics. The latter one is preferable as it has in our opinion more general implications than case studies. Thus, it is necessary to create artificial flight paths.

In the first step, two random points are selected. Equally spaced waypoints are created between the pair of random points to represent a flight track. In this case a uniform distribution is used for the longitude and latitude values of each random point. This means that the waypoints lie along a loxodrome, but since the EU-nest covers only a small part of the globe, which can be considered flat, and the loxodrome is thus quite close to a great circle. The spacing between the waypoints is approximately 0.25° , which corresponds to about 25 km in the mid-latitudes. For each experiment, 1000 random flight paths are constructed in this way. For the sake of simplification, all waypoints are one single flight level (FL), in this case FL 350. Instead of taking the same grid point as in the previous section, the next possible grid point is taken via the nearest-neighbour method for each waypoint. The approach for comparing two predictions in this way remains otherwise identical.

3.2.4 Scores

For further processing of the data, a contingency table is used. The contingency table can be further reduced to the CSI (*Critical Success Index*) and the ETS (*Equitable Threat Score*). The CSI is defined in equation 3.2 and the ETS in equation 3.3. Table 3.1 shows the different meanings of the variables used in a contingency table.

$$\text{CSI} = \frac{a}{(a + b + c)} \quad (3.2)$$

$$\text{ETS} = \frac{(a - a_r)}{(a + b + c) - a_r} \quad (3.3a)$$

$$a_r = \frac{(a + b)(a + c)}{(a + b + c + d)} \quad (3.3b)$$

If one is interested in the forecast and observation of ice supersaturation, the case where it is neither forecast nor observed is generally the most frequent one, thus d in the contingency table is here the largest but least important parameter. This has to be taken into account when choosing a score. CSI (*Critical Success Index*) and ETS (*Equitable Threat Score*) are scores that do not place much weight on d . The CSI can roughly be understood as the fraction of correct forecasts within the interesting events (false negative, false positive, and correct forecasts). The CSI ranges between 0 and 1. A high score is desirable, as it means that the percentage of correct forecasts is high. However, even if the forecasts were made in a random fashion, a certain proportion of correct forecasts would occur by chance. This effect is corrected for in the ETS where the count a for correct forecasts is reduced by a_r , the expected number of correct forecasts in a purely random forecast. The ETS ranges from $-1/3$ to 1. Negative ETS implies that the forecast is more often wrong than a purely random forecast, which in turn has ETS = 0. ETS = 1 would signify a perfect forecast.

Table 3.1 Sketch of a contingency table.

	observed		
	True	False	
predicted	True	b	a+b
	False	d	c+d
	a+c	b+d	a+b+c+d

3.2.5 Maximum random overlap

For each waypoint, the nearest grid point is used to represent the *PPC*-field at the waypoint. We use a similar method to choose cloudiness (*CLC*) but instead of taking a single pressure level, we consider cloud coverage in the entire upper troposphere ($50 \leq p \leq 400$ hPa). This was done because the high cold clouds can overshadow the ERF of contrails. To compress the cloud coverage of the whole upper tropospheric column into a single number, an effective cloud cover, we use the maximum random overlap method.

The maximum random overlap method is a simple method to calculate the effective cloud cover in an atmospheric column over several model levels. This method can be found in various papers [19, 33, 27].

Two assumptions are made for this method. Firstly, it is assumed that the clouds in adjacent model levels belong to one large cloud. This kind of large cloud is called in the following a cloud group. Another assumption is that these clouds within a cloud group overlap as much as possible, which means that the maximum cloud fraction in the considered levels equals the cloud fraction of the cloud group that covers the levels.

Two cloud groups separated by a model level with coverage 0 are assumed to overlap randomly. For each of these n cloud groups, the maximum cloud cover B_k within the k -th cloud group is taken from the maximum of all model levels within the cloud group. The total cloud cover B_{tot} is then calculated using equation 3.4. The cloud-free area is determined first using the product of all $(1 - B_k)$. The difference between the total area (1) and the cloud-free area gives the total degree of coverage.

$$B_{tot} = 1 - \prod_{k=1}^n (1 - B_k) \quad (3.4)$$

3.3 Experiments conducted

WAWFOR data are issued every 6 hours with hourly resolution up to a 48 hours forecast. This implies that the weather forecast of a certain hour on a given day can be found in various forecast runs with varying lead times. The most recent forecast with fully developed ice supersaturation and with shortest lead time to a certain hour will be used as a proxy of reality, since observations of *PPC* are not possible. In this case here, it is zero to six hours for the one-moment scheme (i.e., WAWFOR-Klima-1 dataset) and 7 to 12 hours for the two-moment scheme (i.e., WAWFOR-Klima-1s dataset).

An older forecast with a longer lead time will represent the time when the flights were planned strategically. Lead times of up to 30 hours are considered, a number chosen considering common circumstances in strategically planned rerouting. Climate-aware flight planning takes place several hours, say 3 to 10 hours, before takeoff. The weather forecast at the time of flight routing may already be 10 hours old, since it is initialised at certain times and then needs about 4 hours to complete. The flight itself can last 10 hours. This means that the temporal distance between the initialisation of the weather forecast and the actual time when the aircraft is en-route, the lead time, may reach 24 hours or, in extreme cases, even 30 hours.

The question is now how the assimilation of more and more observations into the subsequent weather simulations changes the forecasts and how these changes affect the desired success of strategically planned contrail-avoidance routings.

This thesis evaluates the differences between multiple forecasts for the same time but with different lead times. For this comparison, the methods described in section 3.2 are used. Before we compare different forecasts, we first consider the uncertainty of a single forecast, which is expressed by the differences between the deterministic and the ensemble calculation. For cases with $PPC = 1/0$ in the deterministic run, we study the respective distribution of PPC_prob . We repeat this exercise with different lead times for the same unique valid time. First, we present histograms, but then we proceed to correlations, with the aim of compressing complex information into a single value, which is easier to interpret. In order to show a statistically relevant development over time, 26 independent cases (between the end of October and March) are plotted for different lead times (up to 42 hours). This is done once for the autocorrelation of PPC and for the cross-correlation of PPC and PPC_prob . For each case, the PPC field with a lead time less than 6 hours is the proxy of reality with which the comparison is made.

Next, a case is examined with the random flight method using a difference of 24 hours between the two forecasts. We furthermore show a particular good and bad situation using the method from section 3.2.2. After that, a global horizontal cross section is displayed using the same method. We not only consider the forecasts on a single flight level but also one vertical cut, a perspective that is important for vertical rerouting.

In the next step, we consider 29 times (between the end of October and the end of April) and different lead times to gain a more general insight by applying statistics. So far, data from the one-moment microphysics scheme are used, but in an analysis of the temporal change of certain score values (see below), data from the two-moment experiments are employed as well as data from the one-moment scheme and it will turn out that the score values of these two models are more or less indistinguishable. The 30 days (between March and May) used from the Klima-1s data are chosen independently of the 29 days from the Klima-1 data. The comparison is here over the whole 3D-field and not only over one flight level as in the previous statistical analysis.

Finally, the natural cloudiness is analysed in the four categories (correct positives/negatives, false alarms, and misses). For that purpose, another 32 independent cases are chosen out of three months (between April and June). This analysis is motivated by the observation that contrails often appear in the neighbourhood or even intermixed with natural cirrus, which modifies their radiation effects.

Chapter 4

Results and Discussion

In this chapter we are going to assess the data under multiple aspects. In the first part, we shall inspect the variables ppc , ppc_prob and their relations between each other. To this end, we use conditional probability distributions, correlations and their evolution over time. In the next part, we investigate the influence of an imperfect weather forecast on strategic flight planning regarding contrail avoidance. We therefore analyse Venn-diagrams with four different cases (correct positives, correct negatives, misses, and false alarms).

The sections 4.2 are taken from the paper [88] in a slightly modified form. These sections were written in collaboration between the authors Klaus Gierens and Georg von Bonhorst. The texts were changed so that they fit better into the structure of the Master's thesis. The figures 4.9, 4.10, 4.12 and 4.13 were plotted by Moritz Maizet as part of an internship. He was supervised by the other authors of the paper [88] and contributed these graphs to the paper.

4.1 Ensemble vs. deterministic forecasts of potential contrail cover

The "Klima1" datasets have an ensemble and a deterministic version of the new variable potential persistent contrails (PPC and PPC_prob). Since both PPC and PPC_prob describe the same atmospheric situation, it is interesting to see how the two situations ($PPC = 1$ or 0) in the deterministic forecast are reflected in the ensemble.

First, we inspect one forecast for one point in time (valid time) and plot the distribution of PPC_prob under the condition that ppc is 0 (figure 4.1) or 1 (figure 4.2). We arbitrarily chose the 23th October 2024 19:00UTC.

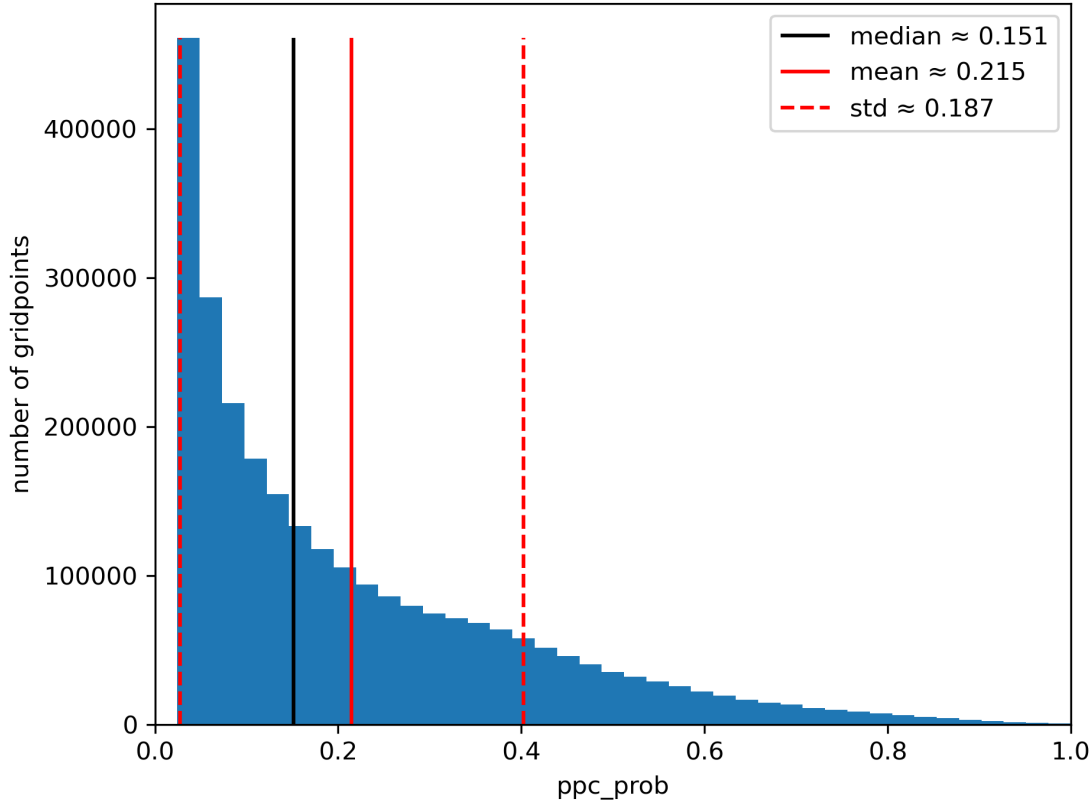


Figure 4.1 Histograms of PPC_prob under the condition that PPC is zero and PPC_prob larger than zero. The black solid line is the truncated median, the red solid is the truncated mean, and the red dashed lines show the truncated standard deviation. The truncation is necessary, otherwise all statistical measures would appear in the first bin, rendering this representation useless. This behaviour is due to the fact that the state where the conditions for $PPC = 0$ met is by far the most common state in the troposphere. The zero bin alone would have over 90% of the gridpoints. The data set used is from the latest weather forecast for 2023-10-25T1900 UTC.

Of the more than 52 million grid points in one forecast, only around 4 million (2.4 million in figure 4.1 and 1.6 million in figure 4.2) contribute to the two diagrams. As indicated previously, this is due to the fact that there is usually no ice supersaturation in the atmosphere. Since the ensemble members can reflect part of the uncertainties via their spread, it can be seen in both figures that not all ensemble members predict the same as the deterministic run, and thus the forecast has some uncertainties. There are even several points where more than half of the ensemble members predict the opposite of the deterministic forecast.

Figure 4.1 shows the distribution of PPC_prob for all gridpoints where $PPC = 0$, that is where contrails are not expected. Most of the ensemble members agree with this expectation at most gridpoints, such that there is a huge peak at $PPC_prob = 0$. This peak contains 90% of the gridpoints in forecast field. This is not surprising, as a situation without ice supersaturation and thus with $PPC = 0$ represents the most common state in the atmosphere [28]. The peak is omitted from the plot in order

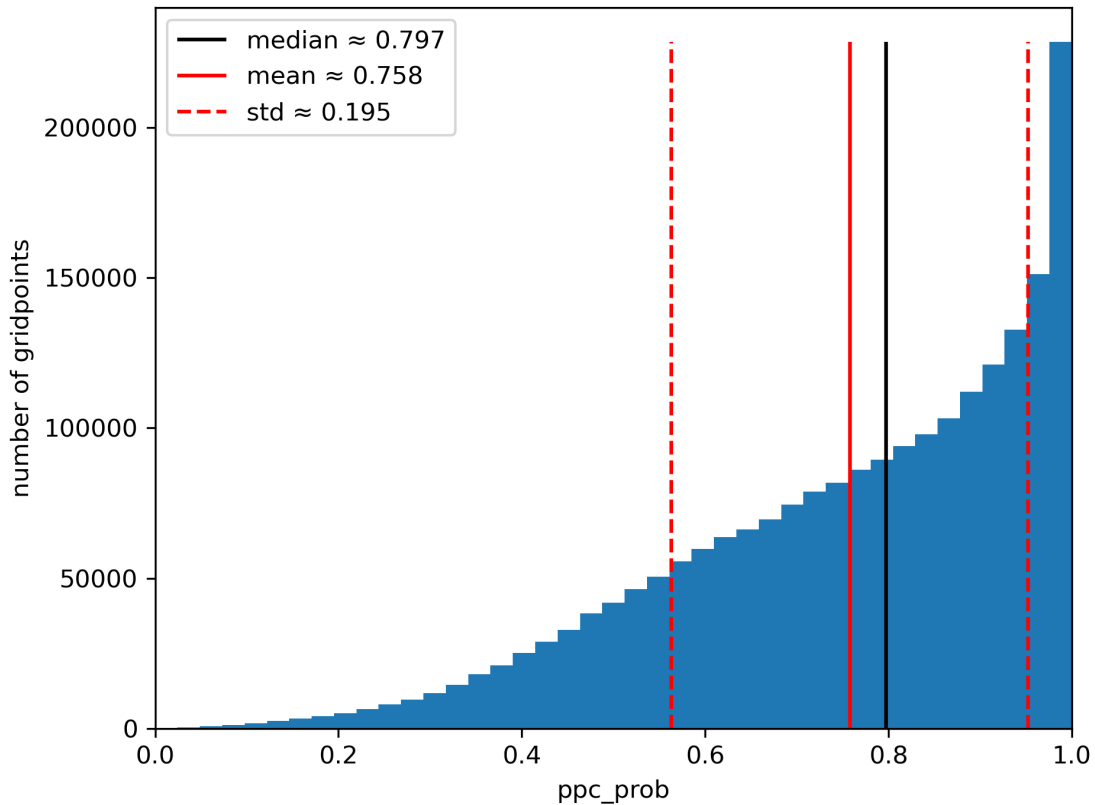


Figure 4.2 As figure 4.1, but under the condition that PPC is one and no bin is omitted.

to make the rest of the distribution visible. In the remaining $PPC = 0$ gridpoints (about 5% of all gridpoints in the forecast field) not all of the ensemble members agree with the deterministic run. But cases with high agreement (PPC_prob small) occur often and cases with low agreement (PPC_prob large) rarely. The distribution of PPC_prob decays roughly in exponential fashion. In this specific case, the truncated (i.e. without PPC_prob) mean value is 0.2. This means that on average over all gridpoints with $PPC = 0$ and $PPC_prob \neq 0$, $1/5$ of all ensemble members don't agree with the deterministic run. The truncated median lies closer to zero at around $1/7$. The truncated standard deviation of this asymmetric distribution, which is skewed toward 0, is about $1/6$.

In contrast to figure 4.1, no grid points are omitted in figure 4.2. In this graph, the distribution of PPC_prob is derived from all points at which PPC is one. Apart from a peak at 1, the distribution looks like a triangle that increases towards 1. In about 10% of the grid boxes with $PPC = 1$, all ensemble members agree. Consequently, in the remaining 90% of $PPC = 1$ gridboxes not all members agree and on average only $3/4$ of the ensemble members agree with $PPC = 1$. The median is close to the average, but is slightly more in the direction of one. The standard deviation of this distribution is about $1/5$.

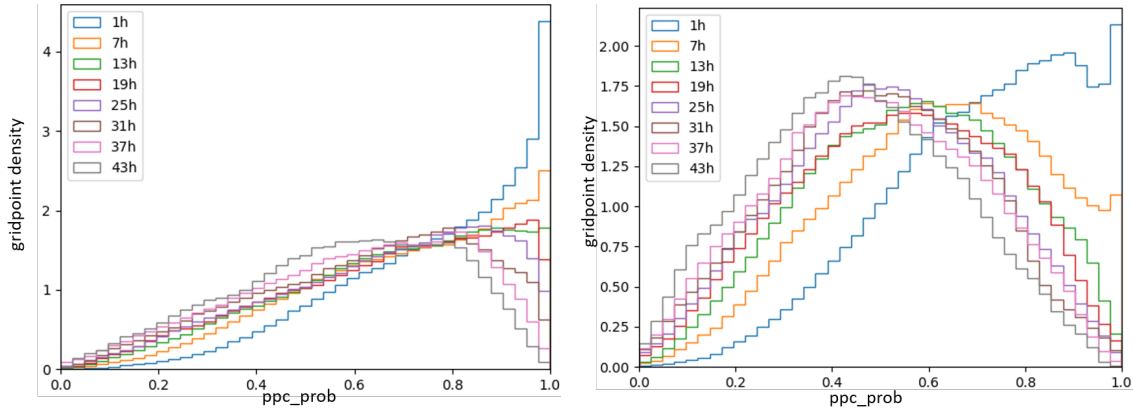


Figure 4.3 Histograms of PPC_prob under the condition that PPC equals one, similar to figure 4.2. Every individual line depicts a different lead time. The date for the left plot is the 25th October 2023 19:00 UTC and for the right one the 25th December 2023 19:00 UTC. The left diagram shows pattern that can be usually found in this kind of diagram, whereas the right one seems to be a more rare case. The spread and distance of the mean in these diagrams is connected to the uncertainty of the weather forecast. It is therefore conceivable that the image on the right-hand side shows a more uncertain forecast. Furthermore, the forecasts get, as expected, more uncertain and spread out for longer lead times.

Given our primary concern is regions with potential consistent contrails, we now analyse the variation in histograms under the condition that PPC equals one across different forecast horizons.

In figure 4.3 on the left side we can see a similar kind of plot as in figure 4.2. The prediction time is the same (23th October 2024 19:00UTC). This can represent an aircraft on route and we want to predict its contrail formation potential, but in this figures there are histograms for different lead times. That is, they belong to forecast with different initialisation times, between 1 and 43 h in the past. The PPC and PPC_prob are always from the deterministic and ensemble runs with identical initialisation time. To make a comparison of different lead times possible, the area under each histogram is normalised to one. For each model run n-hours (1, 7, 13, 19, 25, 31, 37 and 43 h) before the valid time, we plot the density function of PPC_prob under the condition that PPC equals one. Figure 4.3 on the left side is a typical example. The further the model initialisation lies in the past, the flatter is the density function. Furthermore, it is also successively shifted closer to PPC_prob zero. The reason behind this phenomenon is quite simple: In a chaotic yet deterministic model, model runs with slightly different initial conditions spread over time [34]. The PPC_prob is an average of 40 different model runs with slightly modified initial conditions. It is therefore clear that as the delay between the initialisation time and the valid time increases, less and less members of the ensemble agree with the PPC parameter of the deterministic run. The distribution is therefore spread out. The temporal behaviour of the histograms occurs quite often, but there are exceptions.

On the right side of figure 4.3 we see the same kind of plot as on the left. The chosen date was the 25th December 2025 at 19:00 UTC. This was a weather situation that was hard to predict (personal correspondence with Linda Schlemmer, DWD). If we compare the left- and right-hand side of figure 4.3, we see that they have noticeable differences. The 1 h line peaks only half as high as in the other case on the left side of the figure. The peaks of the other runs are more shifted towards 0.5. The histograms look more like a Gaussian distribution and not like a distribution skewed to the right.

Taken together, the results so far suggest that forecast fields are getting worse with larger lead times and there are some peculiar weather situations where prediction of future weather is more difficult.

Until now, we only looked at individual situations. This does not give us an idea of general trends. Since this is desirable, but not feasible, with the diagrams in figure 4.3, we try to capture the connection between different lead times and the two variables PPC and PPC_{prob} via a single number and search for statistical patterns of this number. The algorithm we chose for this is the Pearson correlation, cf. section 3.2.1. The Pearson correlation is a way to describe similarities of variables with only one number. In the next two figures, we chose multiple dates and for each date the PPC field with the shortest lead time as a reference (proxy for reality). We correlate this reference with either variables PPC or PPC_{prob} from forecasts with earlier initialisation times.

In figure 4.4 we plot the autocorrelation of PPC for 26 independently chosen dates between the end of October 2023 and March 2024. These 26 cases are depicted with variously coloured dashed lines. The reference PPC field in each case is from the first five hours of the most recent forecast. These PPC fields are correlated to PPC fields from runs with earlier initialisation time increasing in steps of 6 h, up to 48 h earlier. The 6 h were chosen because this is the timeframe in which a new forecast is calculated with more assimilated measurements. The thicker blue line is the average of these 26 autocorrelation functions, and the blue shaded area is the corresponding standard deviation.

The autocorrelation function starts at 1 per definition (correlation of the proxy with itself) and decreases on average as the lead time gets longer. With increasing lead time the average autocorrelation decreases, reaching ≈ 0.6 at 48 h lead time, and its standard deviation increases to almost 0.1 at 48 h. There are some peculiar cases where the dashed line of an individual case does not completely follow the trend of the mean and instead increases temporarily. This can be seen as a random fluctuation of the system as the general trend for each line is a decrease.

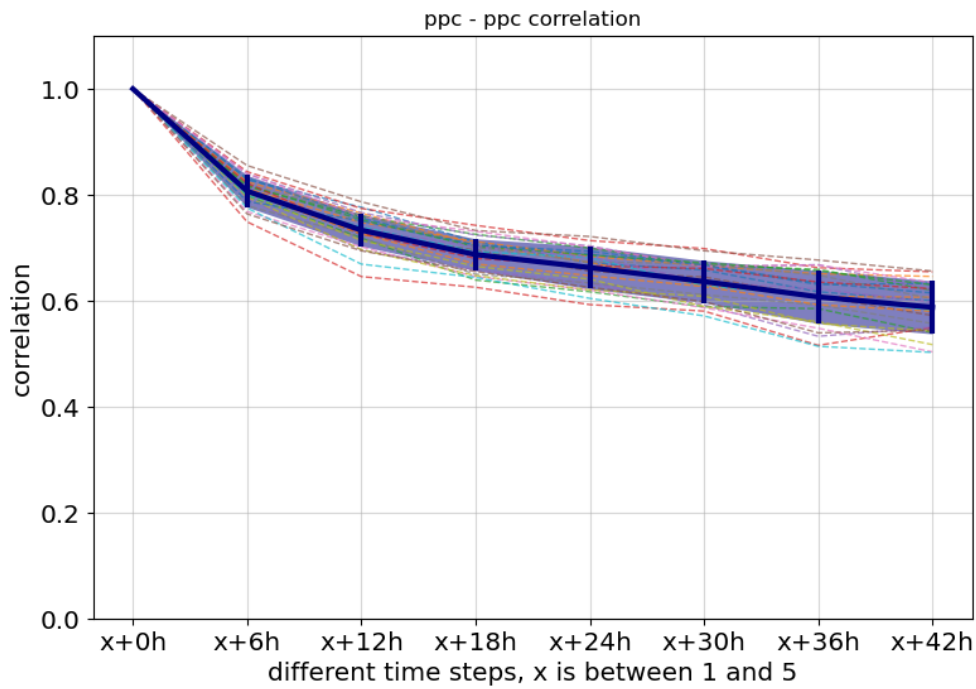


Figure 4.4 Evaluation of the Pearson-correlation between PPC and PPC as a function of lead time. Hereby one PPC is set as a proxy for reality. The dashed colored lines are the result of 26 randomly chosen dates. (Between end of October 2023 and March 2024) The blue solid line is the average and the shaded area indicates the standard deviation. At the beginning all lines start at 1.0, since this is an auto-correlation. The different h stand for the different lead times. As the the lead times get shorter the correlation rises on average. There are some peculiar cases where for a single dashed line this is not the case.

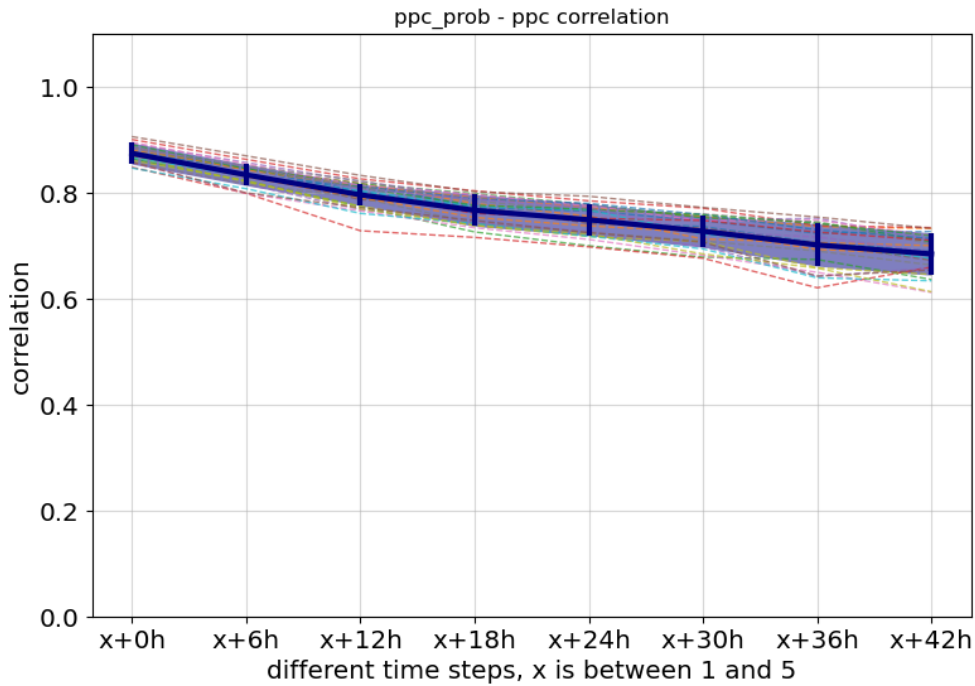


Figure 4.5 This graph shows a similar graph as figure 4.4, but here the *PPC* that is varied is exchanged by *PPC_prob*. The shape of the two figures is very similar, but this figure starts lower and ends higher than the previous one.

The next figure 4.5 is similar to the previous figure. The same days are chosen, but instead of an autocorrelation, a cross-correlation between *PPC* and *PPC_prob* is used. Here, *PPC* with the shortest lead time remains the proxy of reality. The figure design for the individual cases, mean and standard deviation, remains the same. The curve starts slightly below 0.9 at 0 h lead time and ends around 0.7 at 42 h lead time. Here too, the standard deviation increases with longer lead times and there are also small outliers in the individual curves. The crosscorrelation function of *PPC* and *PPC_prob* differs in some respects from the autocorrelation in figure 4.4. *PPC_corr* does not achieve the same agreement as a distribution with itself, but the curve decreases at a lower rate and has a lower standard deviation. At the longest lead times, the cross-correlation is about 0.1 above the autocorrelation. It seems that the ensemble mean is better for predictions that have longer lead times.

Overall, we can conclude from this section: First, *PPC* and *PPC_prob* correlate strongly with each other. Second, shorter lead times achieve higher correlations than longer lead times. Third, the ensemble mean is to be favoured for longer prediction times. Fourth, the correlations are always higher than 0.6. In spite of that, it is not clear whether this is actually a positive result or whether it is rather due to the predominance of cases where no contrail can form. Other studies, like the one in the next section, are necessary, which factor in the high probability of the most

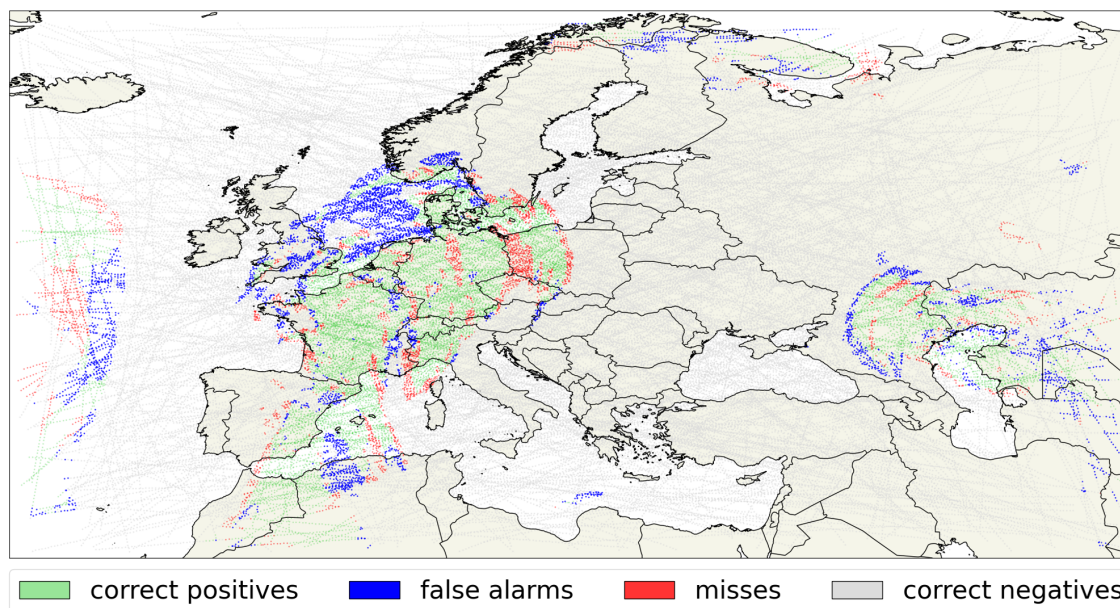


Figure 4.6 1000 random flight tracks on flight level 350 over Europe on 20th March 2024, 11:00 UTC. The single waypoints are coloured according the relation between the contrail forecast with a lead time of 24 hrs and the most recent forecast for the time of the flights. Grey dots: no contrails predicted in both forecasts; green dots: contrails predicted at flight planning and in the most recent forecast; red dots: misses; blue dots: false positives. Note that some regions near the borders of the map are not covered with random flight tracks.

common state.

At this point, we should again point out the limitations of this comparison. The predictions are compared only with one other prediction. Errors between reality/observations and the prediction are not recorded. Therefore, only the "stability" of the prediction is analysed. Furthermore, we only have a very vague idea of how air traffic is affected by the changes in the forecast from the investigations carried out so far. In the next section, which presents the results of the paper, we will take this point into account in our further analyses.

4.2 Strategic contrail avoidance under imperfect weather forecast

4.2.1 Results

Evaluation on a single flight level

Figure 4.6 shows 1000 random flight tracks over Europe for one hour (20th March 2024, 11:00UTC). We assume that the routing of these flights has been planned

Table 4.1 Number of waypoints on the 202403201100

	0+5h True	0+5h False	Σ
24+5h True	18576	6328	24904
24+5h False	5392	101328	106720
Σ	23968	107656	131624

Table 4.2 Number of flown km on the 202403201100 in 1000 km

	0+5h True	0+5h False	Σ
24+5h True	464	158	623
24+5h False	135	2.533	2.668
Σ	599	2.691	3.291

24 hours ago, that is 19th March 2024, 11:00UTC. The most recent forecast available at that time was initialised at 06:00 UTC. This means, the forecast is already 5 hours old at the time of the routing process. At 20th March 2024, 11:00UTC, when the planes are underway, the forecast used for flight planning is tested against the then most recent forecast of 20th March 2024, 06:00UTC, that is, with a lead time of 5 h. For the simplicity of the test we assume that all flights take place on FL (flight level) 350 (about 238.4 hPa). The map of Fig. 4.6 shows the flight tracks in four colours: Grey means that no contrails were expected at flight planning, and no contrails formed according to the most recent weather information. Green means that both forecasts agree on contrail formation, so that contrail avoidance could be beneficial. Blue indicates tracks where contrails have been predicted first, but not so later (false positives); here contrail avoidance measures lead to rerouting along with its penalties, such as additional fuel consumption and emissions, without a benefit of actual contrail avoidance. Finally, red tracks indicate regions where ice-supersaturation appeared only after the initial flight planning (misses). This would lead to the unintentional forming of contrails. The analysis of this special case in numbers of waypoints and in flown distances (in 10^3 km) is given in tables 4.1 and 4.2. Here, flown distances are computed from numbers of waypoints along a track by multiplication of the latter number with 25 km.

For this case, contrails are predicted for $6.2 \cdot 10^5$ km, but rerouting is in vain on $1.6 \cdot 10^5$ km, approximately a quarter of the total predicted contrail distance (false positives). $4.6 \cdot 10^5$ km contrails were correctly predicted, but simultaneously more than $1.3 \cdot 10^5$ km contrails are formed that have not been forecast. This means that about 30% of the contrail distance that has successfully been avoided has been missed at other locations. For this case, the CSI is 0.61 and the ETS is 0.55.

As a further illustration of the range of possible results, we selected two dates, one with a particularly high and one with a quite low CSI at 24 hrs lead time, see

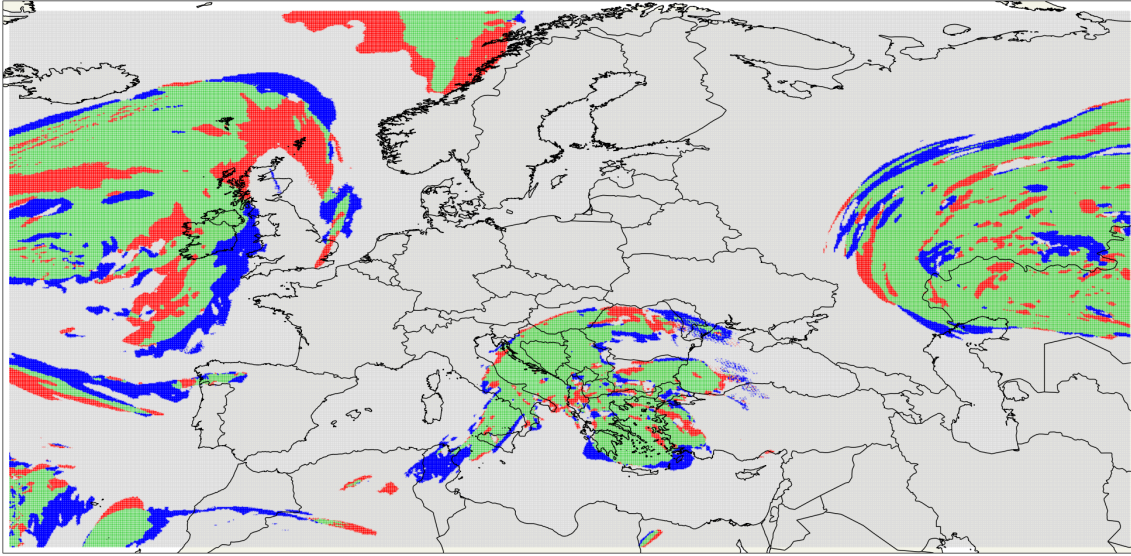


Figure 4.7 Comparison of contrail forecast at two different lead times, one at flight planning (lead time 24 hrs) and one at the time of the flight. Grid-points are coloured as in figure 4.6. The selected date, the 21st November 2023, 14:00 UTC, is one where the forecast gives a high CSI value.

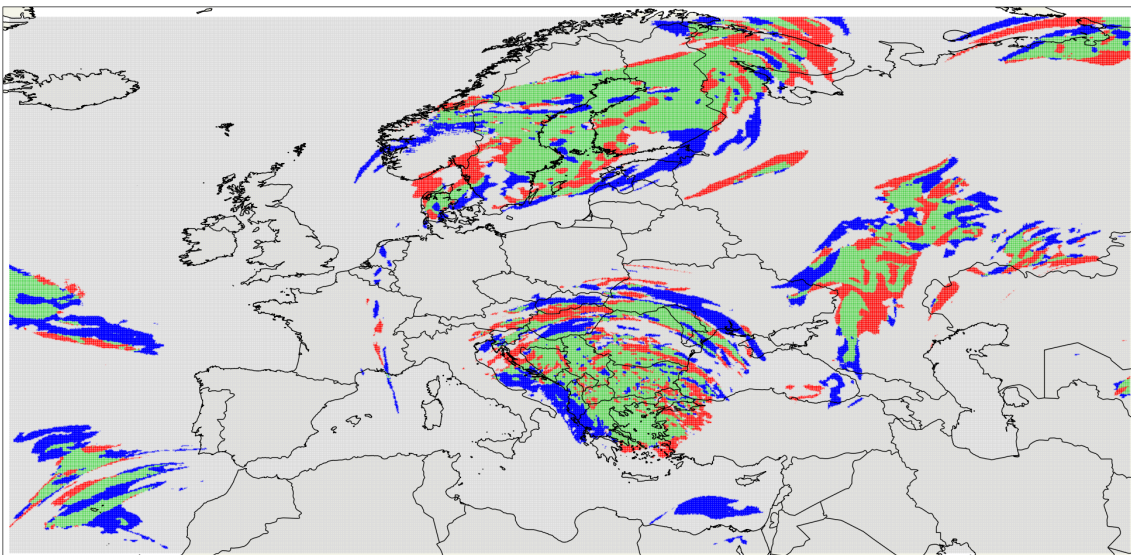


Figure 4.8 As figure 4.7, but for the 29th February 2024, 23:00 UTC, a day that gives a quite low CSI.

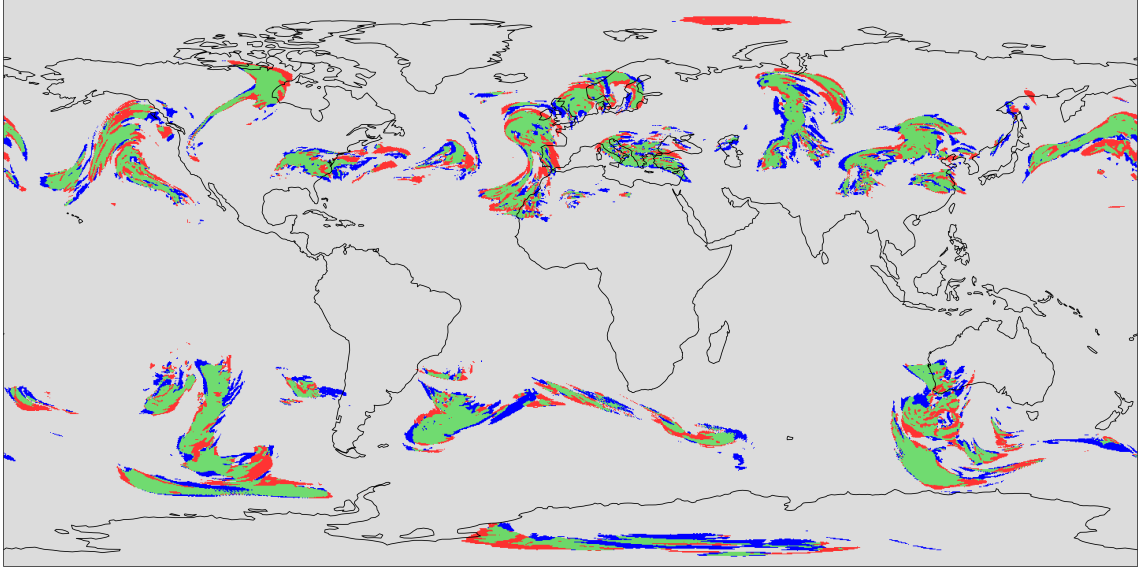


Figure 4.9 As figure 4.7, but global view for FL 350 on 9th May 2024 1:00 UTC. The two forecasts for that time have lead times of 25 and 1 hour, respectively. The colour-code is the same as in the previous figures. Potential contrail formation regions appear in both mid-latitudes and they seem to follow large-scale synoptic weather patterns. Regions where $PPC = 1$ is correctly forecast are generally surrounded by regions where the first forecast could not be confirmed later. Some isolated features with wrong forecasts appear as well.

figures 4.7 and 4.8. Note that these figures are constructed using the simple counting method introduced in section 3.2.2. The colour code is the same as before, and these figures appear quite similar to the figure with the random flight tracks, except for clearer colours since all grid-points are coloured. On the good day (fig. 4.7) there are extended and mostly coherent regions with correct forecasts visible. Also, the regions with wrong forecasts are extended and coherent, both at the edges and within the regions of correct forecasts, but generally smaller. Probably the main reason why the other day is a bad one (fig. 4.8) is that correct and incorrect forecasts are mixed on small scales. This points to intricate small-scale structure with sharp gradients in the underlying humidity field. CSI and ETS can be computed as before and here they are 0.64 and 0.56 for the good day and 0.48 and 0.42 for the bad one.

Figure 4.9 shows a similar situation globally. Potential contrail forming regions on FL 350 are located in the mid-latitudes of both hemispheres. Their curly shape suggests that they somehow follow the jet streams with their embedded synoptic systems. Generally, areas with correct forecasts are surrounded by more or less thick edges with wrong forecasts. However, wrong forecasts not connected to regions with correct positives appear as well.

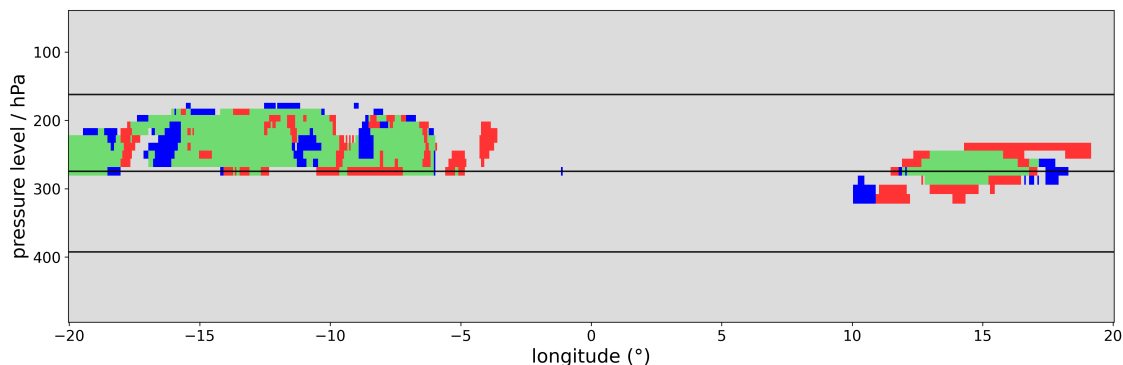


Figure 4.10 Vertical cross-section of $PPC = 1$ grid-boxes in the upper troposphere ($p \leq 500$ hPa) along 47°N from 20°W to 20°E for the 9th May 2024, 1:00 UTC. The colour-code is the same as in the previous figures. The PPC field shows examples where contrail avoidance appears easy (large coherent green areas) and others where it would be challenging (areas where colours are mixed at smaller scales). For orientation, a number of flight levels are indicated as horizontal black lines: FL 430, 320, 240 from top to bottom.

Vertical aspect

In order to demonstrate that the results obtained so far are not confined to a single flight level we show in fig. 4.10 a vertical cross section along 47°N extending from 20°W to 20°E for 9th May 2024, 1:00 UTC. The cross section extends in the vertical from 500 to 50 hPa. There are several examples of correctly forecast $PPC = 1$ regions which are partly mixed with false alarms and misses. The latter are often located at the edges of regions with correct forecasts. Sometimes false alarms and misses occur isolated from other regions, e.g. at 10°E . Misses (red colour) at the lower edges of $PPC = 1$ regions are dangerous because, in contrail avoidance procedures, aircraft often change their flight level to a lower one (because they usually fly as high as possible) where they may fly into an unexpected contrail formation region if that is located just below the region where contrails have been predicted. Such examples can be found in the figure.

Statistical aspects

For a more general (statistical) evidence, the exercise has been repeated for 29 dates which have been selected randomly from WAWFOR data covering 25th October 2023 to 30th April 2024. Additionally to the 24 hrs lead time, shorter and longer lead times are considered as well with 6 hrs being the minimum for Klima-1 data (12 hrs for Klima-1s data using the two-moment scheme) and 42 hrs the maximum. The results, expressed with CSI and ETS, are plotted in figures 4.11 and 4.12, which show the score values as functions of lead time. Let us first consider the result for Klima-1 which is based on the one-moment scheme (fig. 4.11). Generally, forecasts

get, as expected, better with decreasing lead times. For a 24 h lead time, CSI and ETS both range between 0.4 and 0.6 with a few outliers. At the shortest lead time considered, 6 h, the CSI does not exceed 0.8 and the ETS is typically 0.65 with a standard deviation of about 0.05. Both panels show the mean values as black solid lines; the blue shading represents the standard deviation (σ) and the single coloured curves display the single cases. They can be seen in particular where they deviate more than $\pm 1\sigma$ from the mean. The single cases show sometimes peculiar behaviour, with score values even slightly increasing with lead time.

A comparison, using 30 additional randomly chosen forecast pairs from March to May 2024, of the statistical results between the two types of microphysics schemes (Fig. 4.12, one-moment vs two-moment scheme) demonstrates that the forecast errors, expressed via the two scores, are not dependent on the microphysics. This implies also that they cannot be avoided or minimised by better microphysics schemes. The score functions in the two panels of fig. 4.12 for the two microphysics versions are nearly equal and minor differences are probably statistically insignificant.

Consideration of climate impact

The study above considers only contrail avoidance. It does not distinguish between warming and cooling contrails. In principle, to answer such questions one needs to perform radiation calculations for the predicted contrails during their lifetime [e.g. 76, 77], which is beyond the scope of the present thesis. Instead we consider a simple alternative, namely we look whether natural clouds are above and below the predicted contrails. Here, only clouds in the upper troposphere are considered ($p \leq 400$ hPa). Such high cold clouds modify (diminish) the immediate radiation effect of the contrails, since they scatter solar radiation and absorb/re-emit thermal radiation themselves. The scattering of solar radiation by ambient clouds diminishes the visible contrast (e.g. on satellite images) between the contrail and its environment. This reduces the cooling effect of contrails, since solar photons are then back-scattered to space anyway. Ambient high clouds with similar temperature as that of the contrails absorb longwave radiation that originates from the ground or from lower atmospheric layers. This reduces the contrails' warming impact [66, 91]. Inclusion of clouds in the presented maps would enhance the noise in the figures and render the interpretation difficult. Thus, we simply present statistics of the presence of high clouds in the four selected categories, correct forecasts (no and yes), false positives and misses. The statistics has been determined with 32 forecast pairs obtained in three months (independent of the 29 cases selected above). To determine the high cloud cover we use a method that is traditionally employed in weather- and climate models to calculate the effect of clouds on radiative transfer. This is

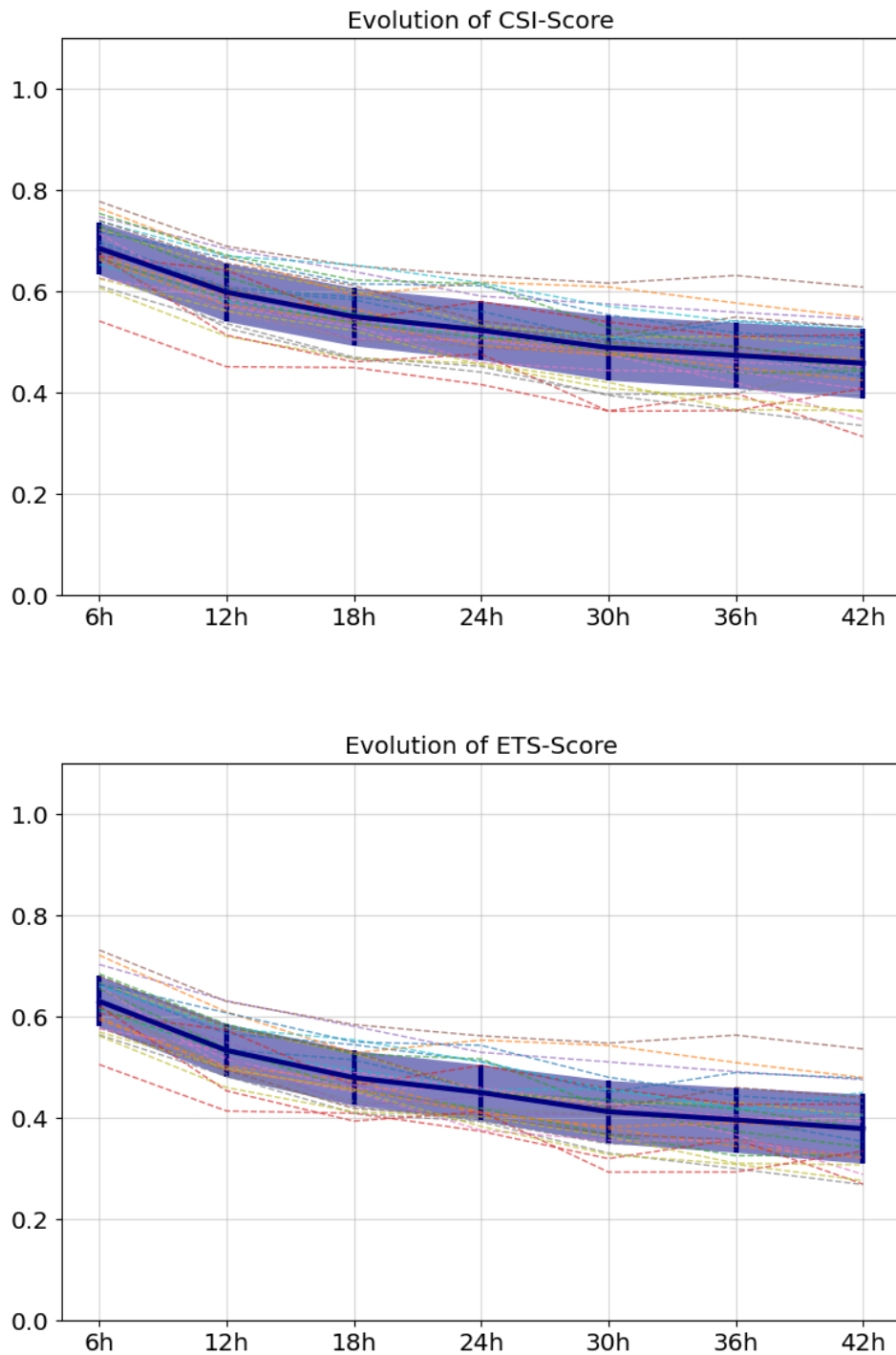


Figure 4.11 CSI (upper panel) and ETS (lower panel) as a function of lead time for flight routing that is intended to avoid contrails. Results are obtained from 29 randomly selected cases. The mean value is represented by the black solid line, and the corresponding standard deviation by blue shading. All 29 single cases are displayed with thin dashed coloured curves which sometimes lie outside of the standard deviation. The results have been obtained from WAWFOR-Klima-1 data, which are based on one-moment microphysics.

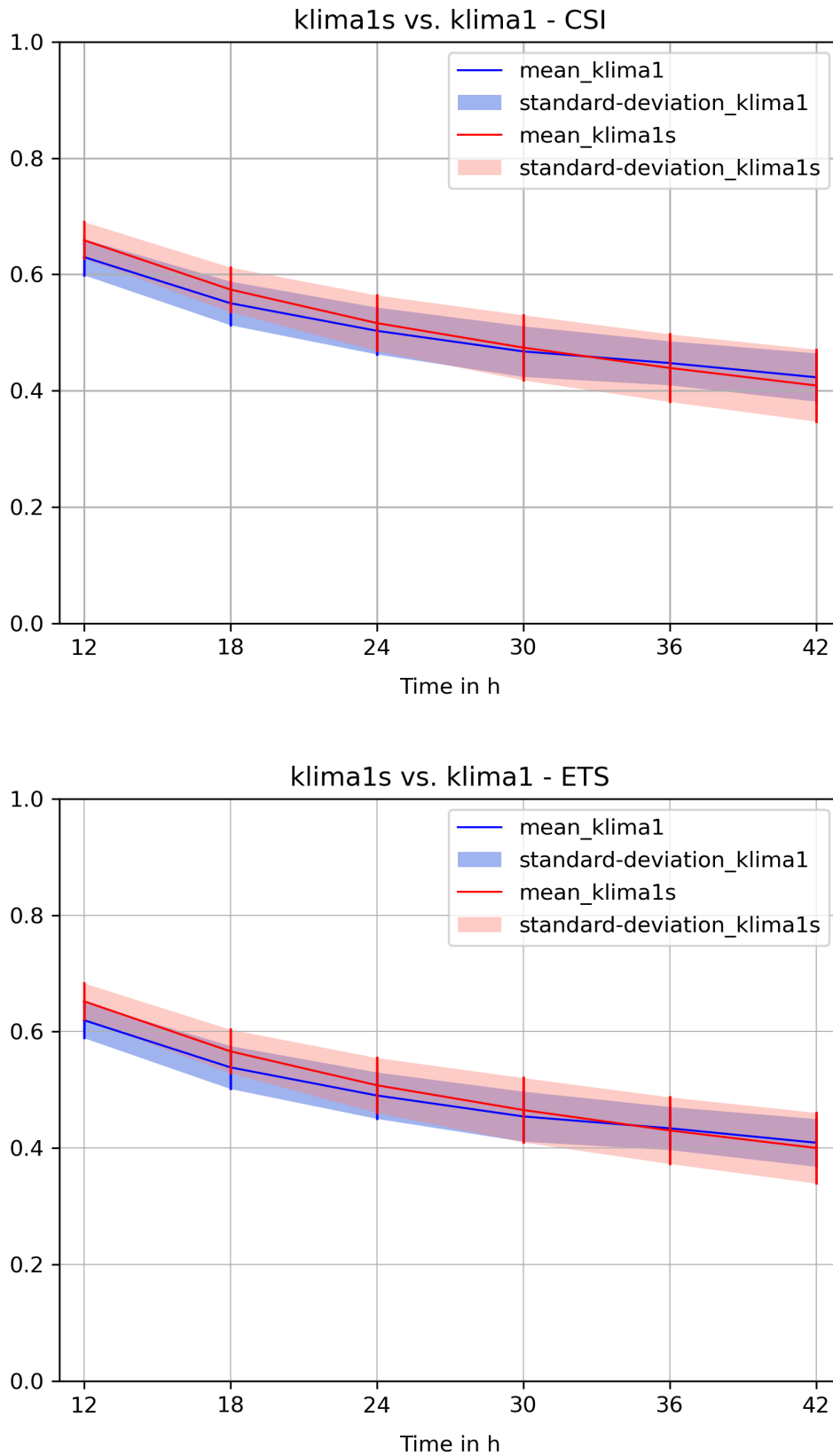


Figure 4.12 Average CSI (upper panel) and ETS (lower panel) of 30 randomly chosen cases for WAWFOR-Klima-1 and WAWFOR-Klima-1s. The two data sets have global coverage but only the EU part as in previous figures is considered. Since the experimental weather simulation using the two-moment scheme needs 6 hrs spin-up, the shortest lead time used for the comparison is 12hrs. The standard deviations of the scores for the two model versions overlap substantially. Minor differences are statistically insignificant.

the so-called maximum-random overlap method [19]. Clouds in adjacent levels are treated as physically coherent, such that their coverage is the maximum of the levels in question. Clouds which are separated by cloud free levels are assumed to overlap randomly. With this method we determine the fractional high-cloud coverage for each lon/lat coordinate in the pressure range $50 \leq p/\text{hPa} \leq 400$. Figure 4.13 (upper panel) shows the result, namely the distribution of the cloud fraction at the times of the flights. All histograms share a U-shape (many cases at the low and high ends, few cases in the middle), which is a result of the high spatial resolution of the data; a small grid box is most often either completely clear or completely covered. The interesting features are thus the ends of the histograms. Most striking is the cloudiness distribution in the regions where contrails are predicted and confirmed: More than half of these grid points have a quite high cloud fraction exceeding 90%, which implies that the correctly predicted contrails do not have the full radiative effect compared to contrails in clear sky. False negatives (misses), that is, regions where in the course of time between the initial forecast and the flight time new ice supersaturation appears, have a large fraction of high cloudiness as well in almost half of the cases. In contrast, the correct negatives have most often (about 70%) a very small cloud fraction. In the false-alarm regions almost cloud free cases occur at about 40% of the grid boxes while overcast cases appear with half that frequency.

The average cloudiness situation forecast at the time of flight planning is similar, but not identical (Figure 4.13 lower panel). The forecast cloudiness is similar in the regions with correct predictions (that is, the cloudiness prediction is good there as well). In the regions with wrong predictions, false alarms and misses, the cloudiness forecast changes as well. False alarm regions are predicted to have a higher fraction of high cloud cover than it turns out later at the time of the flights. In contrast, false negative (misses) regions are forecast to have fewer cases with high cloud fractions than they actually have later at flight time. More specifically, misses areas are predicted to have low cloud cover in about 35% of the cases, while high cloud cover is predicted in approximately 25%. Later, the probability of high clouds increases at such grid points, reaching about 40% while the probability of low cloudiness decreases to less than 20%. The contrary is observed for the grid points with false alarms. From the initial forecast, one expects much more overcast than clear cases (50% and less than 20%), but later the situation is turned upside down: the probability of high cloud cover is reduced to about 20% while the probability of low coverage increases to 40%.

It seems that natural high clouds and contrails behave similarly, which is physically plausible. A possible interpretation of this comparison is that clouds exert a damping effect on the contrail prediction system: Wrong predictions are less damaging and

correct predictions are less beneficial in terms of climate effect in cloudy situations than they would be if the sky were always clear.

4.2.2 Discussion

The simple analysis that has been performed is based on a number of assumptions that need to be discussed further in this section. Questions could arise on the applied methods (see below) and on the relevance to other forecast products. Finally, without interpretation, the scores are just numbers and we need to discuss how large they need to be for a good forecast.

Discussion of the methods applied

The random flights in the analysis are not real flights. This is not a disadvantage of the method. A real flight plan would suffer from the problem of representativity: it would yield a quantification for a special situation, but not allow general statements. The random-tracks method allows to cover the weather maps almost completely as soon as a sufficiently large number of tracks is selected. A real flight plan with less flights would also lead to more noise in the results (e.g. sampling noise); in lucky situations the score values can be better than shown here, but the contrary situation can occur as well. It might look strange to have all these tracks on the same flight level, but this restriction could be lifted. The analysis can be performed for any flight level, and, as shown, it is not necessary at all to consider flight-tracks, it suffices to consider the change of the prediction at single grid points on any flight level. The latter method also avoids a sampling problem that might incur with and depend on the method to construct the random flight paths, a problem that is known as "Bertrand's paradox" [5]. The main advantage to use pseudo flight-tracks is that they look like flight-tracks and the result can be expressed in terms of flight distances instead of simple counts of grid boxes.

The seasonal representativity could be an issue since we have no data from August to October available for the study. Whether CSI and ETS are smaller for that season must be tested once enough additional data of the WAWFOR-Klima-1 data set are available.

The real weather at flight time is not exactly known (not knowable, to be more precise). The best that one can achieve is the most recent forecast (or a re-analysis for later investigations, but DWD does not provide re-analyses). The latest forecast has most data assimilated which are available up to the last initialisation of the forecast run. One must admit that both the forecast at flight planning and the later

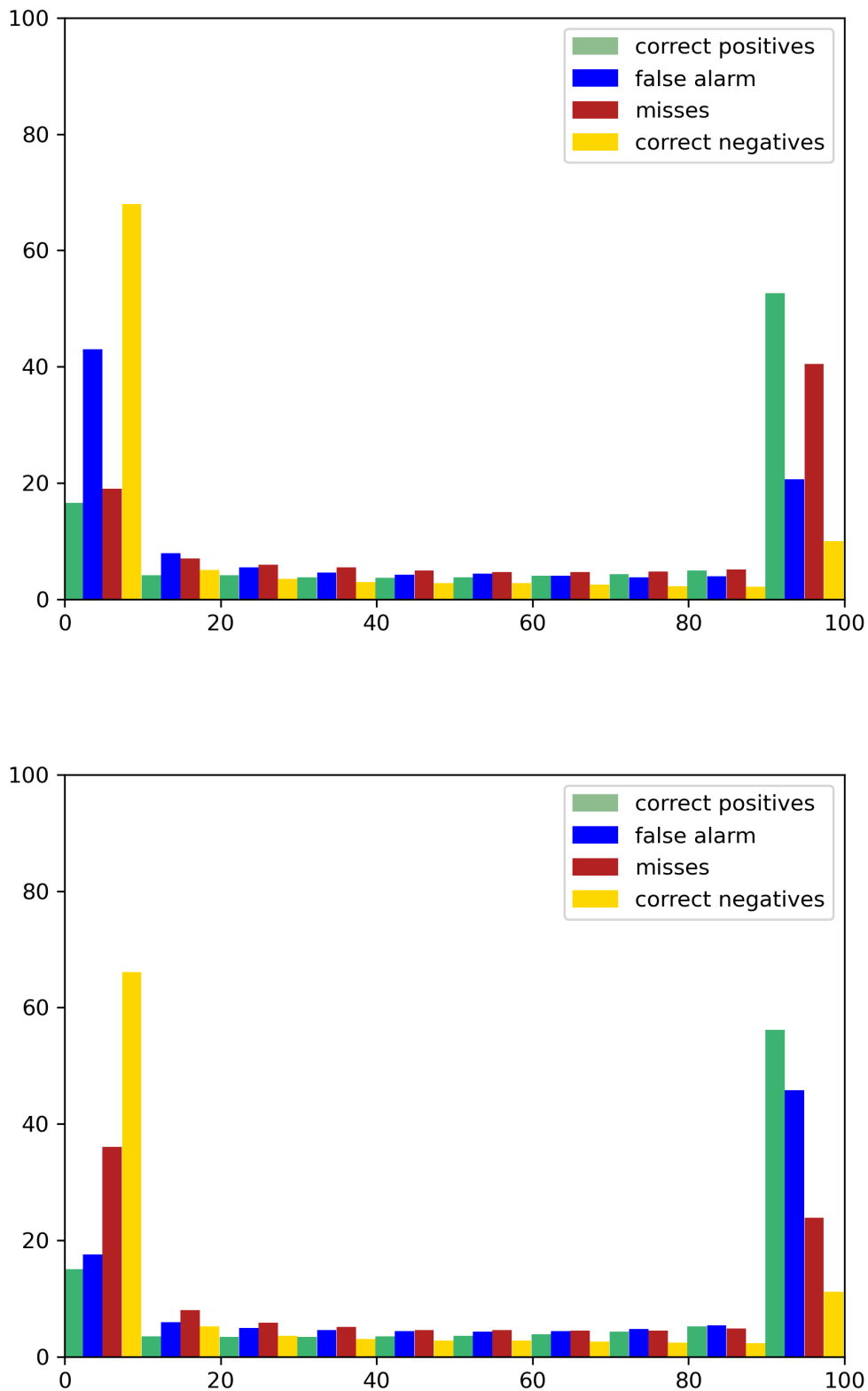


Figure 4.13 Histograms (normalised to 100%) of the maximum-random overlap cloud coverage in the upper tropospheric column (pressure below 400 hPa) at every grid point for each category of contrail forecasts, correct positives and negatives, false positives and misses, see colour code in the inset. Data of 32 randomly chosen forecast pairs are analysed. The data are evaluated at the time of the assumed flights (upper panel) and at the time of flight planning, that is, 24 h before the flights (lower panel).

one at flight time are uncertain representations of the atmospheric reality. Weather centres usually illustrate and quantify this uncertainty using ensemble prediction. Instead of a single (deterministic) forecast a suite of forecasts with slightly perturbed initial conditions are run. One could thus compare all ensemble members from the first forecast to all ensemble members from the second, calculate CSI and ETS for each combination and take mean values and variances. The latter variance increases the total variance due to the sampling of a number of different days. A explicit calculation can be found in the Appendix of the paper [88]. Thus, the real standard deviations of CSI and ETS exceed those shown in figs. 4.11. Although we did not consider these uncertainties, one should be aware of them.

Relevance

For the present analysis we used forecasts of potential contrail formation regions (which involves the Schmidt-Appleman criterion and ice supersaturation) provided *via* the WAWFOR-Klima-1 and Klima-1s datasets by the German weather service, products based on ICON forecast simulations. The question arises whether the results obtained can be expected in a similar way for forecasts issued by other weather models as well. The atmosphere is a system with nonlinear dynamics which causes, for instance, limits to the predictability of the weather and its features. This is a general problem that therefore every weather forecast model has to cope with, not only ICON. The problem is not restricted to the forecast of ice supersaturation and potential contrail occurrence. It also might be aggravated by the nonlinear cloud microphysics and by the fact, that ice-supersaturation is a binary field with a sharp, noncontinuous transition. This sharp dichotomous classification cannot be avoided. Meteorology suffers from related problems in the field of rain forecasts, or, prediction of fronts and locations and intensities of low-pressure systems, just to mention applications that are independent of cloud microphysics. For instance, Hogan et al. [32] verify forecasts of cloud fraction for seven models and show that all models have similar score values (in this case, Peirce Skill Score). They show as well that the scores increase for shorter lead times, that is our results parallel theirs. These problems are obviously general in nature and all weather models suffer from them. Weather models that do not represent ice-supersaturation in their analyses (that is, in the initial fields) even suffer from a spinup problem. This means that the first couple of hours of the forecast are not optimal for the purpose. WAWFOR-Klima-1 does fortunately not have a spinup problem, but WAWFOR-Klima-1s has one. Summarising, the problem identified in this paper is expected to prevail in any other weather forecast model as well.

When is a forecast good enough?

The comparisons in this paper lead to score values (CSI and ETS) whose principle interpretation is that higher scores indicate better forecasts. It is important to note that score values can only be computed after the event; they are not available at the time of flight routing to estimate the success of rerouting *a priori*. That is, after contrail avoidance measures have been taken, the score values can be used to estimate whether the forecasts have been better or worse than at other occasions. But it must be stressed that the scores themselves do not give an answer to the simple question "When is a forecast good enough?". To tackle this question, the climate impact of rerouted flights has to be computed using methods like aCCFs [12, 93] or CoCiP [66] twice, once for the weather forecast that was used for flight routing and once for the latest weather forecast (or reanalysis) that is valid at the time of the flight. The difference of the results is the most plausible measure of the impact of weather forecast imperfections on the success of contrail avoidance rerouting. Such differences, obtained for many flights in the same weather situation (i.e. with a single CSI or ETS value) will probably show some spread with some flights diverted successfully and others not. The range of differences will probably be reflected by the score values. The goal must be that on average the rerouted flights still show an overall benefit for climate if the changing weather is taken into account. The range of score values that belong to such situations would then eventually define a range where forecasts can be considered good enough. It is clear that this research program implies quite some effort, but it is the only way to an answer, to our opinion.

Chapter 5

Conclusion and Outlook

The immanent threat of climate change is causing mankind to rethink. This means that ways of reducing the impact on climate are also being sought in air transport. As there will be no revolutionary technical changes to the entire fleet in the immediate future, the first step is to try to reduce the climate effect by means of other short-term measures. One possibility is to avoid warming contrails, which make up a large part of the non-CO₂ effective radiative forcing (ERF). The non-CO₂ are of the same order of magnitude as CO₂ ERF. The paper by Frias et al. [15] shows that situational rerouting is a promising way to greatly reduce the ERF of contrails with only slightly increased fuel consumption. An implicit assumption of this work and some others [3, 58] is that the weather forecast matches the real weather. This work therefore addresses the influence of imperfect weather forecasts on possible rerouting.

Parts of this chapter are taken from the conclusion of the paper von Bonhorst et al. [88]. The text has been slightly adapted to fit better into this thesis.

New weather variables *PPC* and *PPC_prob* which predict whether a persistent contrail will form or not were analysed for their stability for different forecast horizons. *PPC* is a variable for the prediction of possible persistent contrails, a first step in predicting warming contrails. *PPC_prob* is the ensemble version of it.

First, the simple question was considered to what degree the ensemble members agree with the deterministic forecast in cases where *PPC* is either zero or one. This comparison has been performed for a single forecast and a certain valid time with a temporal distance between initialisation time and valid time of 1 h. For *PPC* = 0, which is the predominant state in the upper troposphere. About 90% of the gridpoints the ensemble mean has *PPC* = 0 as well, but for the remaining gridpoints the ensemble mean is above zero. Often *PPC* = 1 occurs in more than one ensemble member, but the more ensemble members have *PPC* = 1, the less

often this occurs. In contrast, the number where all ensemble members of a run agree with the deterministic run if it is $PPC = 1$ is only a small fraction of all gridpoints.

In the next step, we repeat this analysis for longer lead times, we focus on cases where PPC is one and use the same valid time. The histograms in the image 4.3 showed that the ensemble members match less and less with the deterministic run the longer the prediction times are. Often the PPC_prob histograms increase towards $PPC = 1$, but on some dates they show a peculiar behaviour with a peak around $PPC_prob \approx 0.5$ and a decrease towards $PPC_prob \rightarrow 1$. In order to compress the information, which is necessary for statistical analysis, we determine the autocorrelation between a PPC field with a short lead time (proxy for reality) and PPC fields with a longer lead times for the same valid time and a crosscorrelation between a PPC field with a short lead time (proxy for reality) and PPC_prob fields with a longer lead times for the same valid time. In total, two statistics with 29 independent cases between October and March are created. We analyse how the autocorrelation or cross-correlation with PPC_prob of PPC develops for longer lead times.

For both correlations, all values are above 0.6. Both correlations decrease monotonically on average for longer lead times. The curve of the cross-correlation is flatter than that of the autocorrelation. Although the autocorrelation starts at one above the cross-correlation at around 0.9, the autocorrelation goes beneath the cross-correlation and is for the longest leadtimes at around 0.6 whereas the crosscorrelation is at 0.7 there.

We can draw the following conclusions from this. At shorter lead times, PPC and PPC_prob correlate strongly with each other, as expected. The prediction seems clearly distinguishable from a random forecast up to the longest lead times considered, as the correlation is multiple standard deviations above zero which would be expected for a random forecast. Finally, it seems that for longer lead times, longer than 6 h, an ensemble mean leads to better results.

Next in this thesis, we investigated the effect of an imperfect weather forecast on the success of a potential climate impact mitigation effort, contrail avoidance. For this purpose, we considered two weather forecasts for the same actual time, the time at which flights take place, that is, planes are en-route. One of the forecasts has a long lead time and represents the planning phase of the flights. The other one has a very short lead time and gives the best representation of the atmosphere at the time of the flights. First, we considered 1000 randomly created straight flights on a single flight level. These tracks crossed four categories of areas: 1) areas with no contrail formation in both forecasts (correct negatives), 2) areas with contrails predicted

and later confirmed (correct positives), 3) and 4) areas where the forecasts disagree, that is, with false alarms and misses. The 1000 tracks are good for illustration and for measuring flight distances in the four categories of areas, but not actually necessary; it suffices to check for each grid point whether the forecast is stable (correct predictions) or changes (false predictions).

In an example case, on $623 \cdot 10^3$ km planned flight distances persistent contrails were predicted, but occurred actually on $464 \cdot 10^3$ km. Additionally, $135 \cdot 10^3$ km of contrails occurred unexpectedly (misses). The contingency table in this example can be summarised with a CSI of 0.61 and an ETS of 0.55. In such a case, contrail avoidance is feasible, but in our view, the climate benefit of rerouting is not guaranteed. An improvement in the prediction of contrails, shorter lead times, or in-flight rerouting (tactical contrail avoidance using short-term weather forecasts or nowcasting) would be steps towards reducing these uncertainties.

For the sake of more robust statistics, we repeated the experiment for 29 randomly chosen times, each characterised with one pair of forecasts. The average resulting CSI and ETS values are quite similar to the ones of the mentioned example case. We repeated these experiments with shorter forecast horizons to determine how CSI and ETS improve with shorter lead times. At the shortest lead time considered, 6 h, the CSI increases to an average of 0.7, the ETS reaches about 0.6. The same tests have been performed with WAWFOR data that result from forecasts using two-moment microphysics. The results are indistinguishable from the former ones, which are based on the operational one-moment scheme. This shows that the principal problem shown in this paper cannot be solved with better microphysics in the numerical forecast model.

Ice supersaturation and contrail persistence occur often in cloudy skies. High cold clouds modify (diminish) the immediate radiative effect of contrails. In this study, the areas where contrails have been successfully predicted were most often connected to high values of high cloud cover. Cloudiness prediction and contrail prediction correlate between the forecast pairs: In false alarm areas, cloudiness decreased, and in false negatives areas, cloudiness increased between the two forecasts. This implies that on the one hand, correct forecasts lead to a smaller climate benefit, and on the other hand, wrong mitigation action, justified by a wrong forecast, causes smaller climate damage in cloudy than in clear cases.

We obtain the following conclusions:

- Mitigation-efforts in green aviation should consider the impact of imperfect weather forecasts.
- Forecasts get better at shorter lead times. The airlines get every 6 hours a

new forecast and incorporate the latest into their flight planning, but the flight trajectories get rarely updated when newer forecasts become available. However, this should be in principal feasible for climate optimized routing.

- Clouds are often in the neighbourhood of contrails and modify the irradiative impact. This needs to be considered in avoidance measures as it probably weakens both benefits and disadvantages of the contrail avoidance measures.
- The applied method can principally be used to analyse the climate gain or loss of real flight experiments, such as the test flights currently being conducted by German airlines. The analysis can even be extended to effects of gaseous emissions like NO_x and others, applying the algorithmic response functions [12, 93].

Open points for further research are inter alia:

- Rerouting was not modelled here, but it should be tested whether rerouting (vertically ± 2 FL) leads indeed into non-ISS regions (acc. to forecast) or not (acc. to analysis).
- Further improvement of the forecast of the upper tropospheric humidity fields, including their ice supersaturated parts, for example through assimilation of *in situ* RHi data and utilisation of other data like ground-based camera images is necessary.
- The study should be repeated with real flight trajectories in combination with satellite imagery of contrails and further measurements.

The presented forecast errors have their origin in the nonlinear nature of atmospheric motions. The effects are inevitable, but might be reducible with more data assimilation. In particular, the dynamical nonlinearities are present independently of the cloud parameterisation used in the NWP model.

List of Figures

2.1	Interface between two phases of water depicted in a thermodynamic way	9
2.2	T-e phase diagram of contrail formation	12
3.1	Sketch of a Venn diagram	19
4.1	Histograms of PPC_{prob} under the condition that PPC is zero . . .	26
4.2	Histograms of PPC_{prob} under the condition that PPC is one	27
4.3	Two histograms of PPC_{prob} under the condition that PPC equals one for multiple lead times	28
4.4	Evaluation of the Pearson-auto-correlation of PPC over time	30
4.5	Evaluation of the Pearson-cross-correlation between PPC_{prob} and PPC as a function of lead time	31
4.6	Horizontal cross-section using the random flight method	32
4.7	Horizontal cross-section using the gridpoint method with a quite high CSI	34
4.8	Horizontal cross-section using the gridpoint method with a quite low CSI	34
4.9	Global horizontal cross-section using the gridpoint method	35
4.10	Vertical cross-section using the gridpoint method	36
4.11	CSI and ETS as a function of lead time for the WAWFOR-Klima-1 dataset (EU)	38
4.12	CSI and ETS as a function of lead time for the EU-part of the WAWFOR-Klima-1 dataset (global) and WAWFOR-Klima-1s dataset (global)	39

4.13 Histogram of the the maximum-random overlap cloud coverage in the upper tropospheric column	42
---------------------------------------------------------------------------------------------------------------	----

List of Tables

3.1	Sketch of a contingency table.	21
4.1	Number of waypoints on the 202403201100	33
4.2	Number of flown km on the 202403201100 in 1000 km	33

Bibliography

- [1] John David Anderson and Mary L. Bowden. *Introduction to flight*, volume 582. McGraw-Hill Higher Education, 2005.
- [2] H. Appleman. The formation of exhaust condensation trails by jet aircraft. *Bulletin of the American Meteorological Society*, 34(1):14 – 20, 1953. doi: 10.1175/1520-0477-34.1.14. URL https://journals.ametsoc.org/view/journals/bams/34/1/1520-0477-34_1_14.xml.
- [3] D. Avila, L. Sherry, and T. Thompson. Reducing global warming by airline contrail avoidance: A case study of annual benefits for the contiguous united states. *Transportation Research Interdisciplinary Perspectives*, 2:100033, 2019. doi: 10.1016/j.trip.2019.100033.
- [4] S. Bakan, M. Betancor, V. Gayler, and H. Graßl. Contrail frequency over europe from noaa satellite images. *Annales Geophysicae*, 12:962–968, 1994. doi: 10.1007/s00585-994-0962-y.
- [5] Joseph Bertrand. *Calcul des probabilités*. Gauthier-Villars, 1889.
- [6] Marius Bickel, Michael Ponater, Lisa Bock, Ulrike Burkhardt, and Svenja Reineke. Estimating the effective radiative forcing of contrail cirrus. *Journal of Climate*, 33(5):1991–2005, 2020. doi: 10.1175/JCLI-D-19-0467.1. URL <https://journals.ametsoc.org/view/journals/clim/33/5/jcli-d-19-0467.1.xml>.
- [7] A. Bier, S. Unterstrasser, J. Zink, D. Hillenbrand, T. Jurkat-Witschas, and A. Lottermoser. Contrail formation on ambient aerosol particles for aircraft with hydrogen combustion: a box model trajectory study. *Atmospheric Chemistry and Physics*, 24(4):2319–2344, 2024. doi: 10.5194/acp-24-2319-2024. URL <https://acp.copernicus.org/articles/24/2319/2024/>.
- [8] Ulrike Burkhardt and Bernd Kärcher. Global radiative forcing from contrail cirrus. *Nature climate change*, 1(1):54–58, 2011.

- [9] Ulrike Burkhardt, Bernd Kärcher, and Ulrich Schumann. Global modeling of the contrail and contrail cirrus climate impact. *Bulletin of the American Meteorological Society*, 91(4):479 – 484, 2010. doi: 10.1175/2009BAMS2656.1. URL https://journals.ametsoc.org/view/journals/bams/91/4/2009bams2656_1.xml.
- [10] Reynard de Vries, Rob E. Wolleswinkel, Maurice Hoogreef, and Roelof Vos. *A New Perspective on Battery-Electric Aviation, Part II: Conceptual Design of a 90-Seater*. American Institute of Aeronautics and Astronautics, 2024. doi: 10.2514/6.2024-1490. URL <https://arc.aiaa.org/doi/abs/10.2514/6.2024-1490>.
- [11] N.C. Dickson, K.M. Gierens, H.L. Rogers, and R.L. Jones. Probabilistic description of ice-supersaturated layers in low resolution profiles of relative humidity. *Atmos. Chem. Phys.*, 10:6749–6763, 2010.
- [12] S. Dietmüller, S. Matthes, K. Dahlmann, H. Yama-shita, A. Simorgh, M. Soler, F. Linke, B. Lührs, M.M. Meuser, C.M. Weder, V. Grewe, F. Yin, and F. Castino. A python library for computing individual and merged non-co2 algorithmic climate change functions: Climaccf v1.0. *Geosci. Model Dev.*, 16: 4405–4425, 2023. doi: 10.5194/gmd-16-4405-2023.
- [13] Günther Doms, Jochen Förstner, E Heise, HJ Herzog, Dimitri Mironov, Matthias Raschendorfer, T Reinhardt, Bodo Ritter, R Schrodin, Jan-Peter Schulz, and G Vogel. A description of the nonhydrostatic regional cosmo model. part ii: Physical parameterization. *Deutscher Wetterdienst, Offenbach, Germany*, September 2021. doi: 10.5676/DWD_pub/nwv/cosmo-doc.6.00.II.
- [14] Christine Fichter, Susanne Marquart, Robert Sausen, and David S. Lee. The impact of cruise altitude on contrails and related radiative forcing. *Meteorologische Zeitschrift*, 14(4):563–572, 09 2005. doi: 10.1127/0941?2948/2005/0048. URL <http://dx.doi.org/10.1127/0941?2948/2005/0048>.
- [15] A Martin Frias, M L Shapiro, Z Engberg, R Zopp, M Soler, and M E J Stettler. Feasibility of contrail avoidance in a commercial flight planning system: an operational analysis. *Environmental Research: Infrastructure and Sustainability*, 4(1):015013, mar 2024. doi: 10.1088/2634-4505/ad310c. URL <https://dx.doi.org/10.1088/2634-4505/ad310c>.
- [16] T. M. Fritz, S. D. Eastham, R. L. Speth, and S. R. H. Barrett. The role of plume-scale processes in long-term impacts of aircraft emissions. *Atmospheric Chemistry and Physics*, 20(9):5697–5727, 2020. doi: 10.5194/acp-20-5697-2020. URL <https://acp.copernicus.org/articles/20/5697/2020/>.

- [17] Hutchings G., W. David A. Almena, G. Gratton, D.S. Lee, M. McManus and A. Morton M.M. Maroto-Valer, M. Muskett, J. Pickett N. Kumar, M. Pourkashanian, M. Rosseinsky, and A.W. Rutherford. *2023: Net zero aviation fuels – resource requirements and environmental impacts. Policy briefing.* The Royal Society, February 2023. ISBN 978-1-78252-632-2.
- [18] Roland Gehrels and Ed Garrett. Chapter 11 - rising sea levels as an indicator of global change. In Trevor M. Letcher, editor, *Climate Change (Third Edition)*, pages 205–217. Elsevier, third edition edition, 2021. ISBN 978-0-12-821575-3. doi: <https://doi.org/10.1016/B978-0-12-821575-3.00011-6>. URL <https://www.sciencedirect.com/science/article/pii/B9780128215753000116>.
- [19] J.F. Geleyn and A. Hollingsworth. An economical analytical method for the computation of the interaction between scattering and line absorption of radiation. *Contrib. Atmos. Phys.*, 52, 1979.
- [20] Scott Geraedts, Erica Brand, Thomas R Dean, Sebastian Eastham, Carl Elkin, Zebediah Engberg, Ulrike Hager, Ian Langmore, Kevin McCloskey, Joe Yue-Hei Ng, et al. A scalable system to measure contrail formation on a per-flight basis. *Environmental Research Communications*, 6(1):015008, 2024. doi: 10.1088/2515-7620/ad11ab. URL <https://dx.doi.org/10.1088/2515-7620/ad11ab>.
- [21] Thomas Gerz, Tilman Dürbeck, and Paul Konopka. Transport and effective diffusion of aircraft emissions. *Journal of Geophysical Research: Atmospheres*, 103(D20):25905–25913, 1998. doi: <https://doi.org/10.1029/98JD02282>. URL <https://agupubs.onlinelibrary.wiley.com/doi/abs/10.1029/98JD02282>.
- [22] A. Gettelman and C. Chen. The climate impact of aviation aerosols. *Geophysical Research Letters*, 40(11):2785–2789, 2013. doi: <https://doi.org/10.1002/grl.50520>. URL <https://agupubs.onlinelibrary.wiley.com/doi/abs/10.1002/grl.50520>.
- [23] K. Gierens. Theory of contrail formation for fuel cells. *Aerospace*, 8:164, 2021. doi: 10.3390/aerospace8060164.
- [24] K. Gierens and P. Spichtinger. On the size distribution of ice-supersaturated regions in the upper troposphere and lowermost stratosphere. *Ann. Geophys.*, 18:499–504, 2000.
- [25] K. Gierens, U. Schumann, M. Helten, H.G.J. Smit, and A. Marenco. A distribution law for relative humidity in the upper troposphere and lower stratosphere

- derived from three years of MOZAIC measurements. *Ann. Geophys.*, 17:1218–1226, 1999.
- [26] K Gierens, Robert Sausen, Uwe Bauder, Georg Eckel, Katharina Großmann, Patrick Le Clercq, DS Lee, Bastian Rauch, Daniel Sauer, Christiane Voigt, et al. Influence of aviation fuel composition on the formation and lifetime of contrails—a literature review. *CONCAWE Reports*, 24(1):1–91, 2024.
- [27] Klaus Gierens. Transmission formulation for random stacks of clouds. *Meteorologische Zeitschrift*, 01 2023. doi: 10.1127/metz/2023/1186.
- [28] Klaus Gierens, Peter Spichtinger, and Ulrich Schumann. *Ice Supersaturation*, pages 135–150. Springer Berlin Heidelberg, Berlin, Heidelberg, 2012. ISBN 978-3-642-30183-4. doi: 10.1007/978-3-642-30183-4_9. URL https://doi.org/10.1007/978-3-642-30183-4_9.
- [29] Klaus Martin Gierens. Contrails and contrail cirrus. In Richard Blockley and Wei Shyy, editors, *Encyclopedia of aerospace engineering*. American Institute of Aeronautics and Astronautics, Inc., 2010.
- [30] Andrew J Heymsfield, R Paul Lawson, and GW Sachse. Growth of ice crystals in a precipitating contrail. *Geophysical Research Letters*, 25(9):1335–1338, 1998.
- [31] S. Hofer, K. Gierens, and S. Rohs. How well can persistent contrails be predicted? — an update. *Atmos. Chem. Phys.*, 24:in press, 2024. doi: 10.5194/egusphere-2024-385.
- [32] R.J. Hogan, E.J. O’Connor, and A.J. Illingworth. Verification of cloud fraction forecasts. *Quart. J. Roy. Met. Soc.*, 135:1494–1511, 2009.
- [33] Robin J. Hogan and Anthony J. Illingworth. Deriving cloud overlap statistics from radar. *Quarterly Journal of the Royal Meteorological Society*, 126(569): 2903–2909, 2000. doi: <https://doi.org/10.1002/qj.49712656914>. URL <https://rmets.onlinelibrary.wiley.com/doi/abs/10.1002/qj.49712656914>.
- [34] T. M. Hopson. Assessing the ensemble spread–error relationship. *Monthly Weather Review*, 142(3):1125 – 1142, 2014. doi: 10.1175/MWR-D-12-00111.1. URL <https://journals.ametsoc.org/view/journals/mwre/142/3/mwr-d-12-00111.1.xml>.
- [35] David A Hutchins and Douglas G Capone. The marine nitrogen cycle: new developments and global change. *Nature Reviews Microbiology*, 20(7):401–414, 2022.

- [36] Jana Kalová. Vapor pressure of supercooled water. *International Journal of Thermophysics*, 43(11):165, 2022.
- [37] B Kärcher. A trajectory box model for aircraft exhaust plumes. *Journal of Geophysical Research: Atmospheres*, 100(D9):18835–18844, 1995.
- [38] B. Kärcher and F. Yu. Role of aircraft soot emissions in contrail formation. *Geophys. Res. Lett.*, 36:L01804, doi:10.1029/2008GL036694, 2009.
- [39] B. Kärcher, R. Busen, A. Petzold, F.P. Schröder, U. Schumann, and E.J. Jensen. Physicochemistry of aircraft-generated liquid aerosols, soot, and ice particles 2. comparison with observations and sensitivity studies. *J. Geophys. Res.*, 103:17129–17147, 1998.
- [40] Ralph F. Keeling, Arne Körtzinger, and Nicolas Gruber. Ocean deoxygenation in a warming world. *Annual Review of Marine Science*, 2(Volume 2, 2010): 199–229, 2010. ISSN 1941-0611. doi: <https://doi.org/10.1146/annurev.marine.010908.163855>. URL <https://www.annualreviews.org/content/journals/10.1146/annurev.marine.010908.163855>.
- [41] Thomas E. Kent and Arthur G. Richards. Potential of formation flight for commercial aviation: Three case studies. *Journal of Aircraft*, 58(2):320–333, 2021. doi: 10.2514/1.C035954. URL <https://doi.org/10.2514/1.C035954>.
- [42] Kristy J. Kroeker, Rebecca L. Kordas, Ryan Crim, Iris E. Hendriks, Laura Ramajo, Gerald S. Singh, Carlos M. Duarte, and Jean-Pierre Gattuso. Impacts of ocean acidification on marine organisms: quantifying sensitivities and interaction with warming. *Global Change Biology*, 19(6):1884–1896, 2013. doi: <https://doi.org/10.1111/gcb.12179>. URL <https://onlinelibrary.wiley.com/doi/abs/10.1111/gcb.12179>.
- [43] Stephan Langhans, Florian Linke, Peter Nolte, and Volker Gollnick. System analysis for an intermediate stop operations concept on long range routes. *Journal of Aircraft*, 50(1):29–37, 2013. doi: 10.2514/1.C031446. URL <https://doi.org/10.2514/1.C031446>.
- [44] D.S. Lee, D.W. Fahey, A. Skowron, M.R. Allen, U. Burkhardt, Q. Chen, S.J. Doherty, S. Freeman, P.M. Forster, J. Fuglestvedt, A. Gettelman, R.R. De León, L.L. Lim, M.T. Lund, R.J. Millar, B. Owen, J.E. Penner, G. Pitari, M.J. Prather, R. Sausen, and L.J. Wilcox. The contribution of global aviation to anthropogenic climate forcing for 2000 to 2018. *Atmospheric Environment*, 244:117834, 2021. ISSN 1352-2310. doi: <https://doi.org/10.1016/>

- j.atmosenv.2020.117834. URL <https://www.sciencedirect.com/science/article/pii/S1352231020305689>.
- [45] Paul R Lowe and Jules M Ficke. *The computation of saturation vapor pressure*. Environmental Prediction Research Facility, Naval Postgraduate School . . . , 1974.
- [46] Hermann Mannstein, Richard Meyer, and Peter Wendling. Operational detection of contrails from noaa-avhrr-data. *International Journal of Remote Sensing*, 20(8):1641–1660, 1999. URL <https://doi.org/10.1080/014311699212650>.
- [47] Hermann Mannstein, Andreas Brömser, and Luca Bugliaro. Ground-based observations for the validation of contrails and cirrus detection in satellite imagery. *Atmospheric Measurement Techniques*, 3(3):655–669, 2010. doi: 10.5194/amt-3-655-2010. URL <https://amt.copernicus.org/articles/3/655/2010/>.
- [48] A. Marenco, V. Thouret, P. Nedelec, H. Smit, M. Helten, D. Kley, F. Karcher, P. Simon, K. Law, J. Pyle, G. Poschmann, R. Von Wrede, C. Hume, and T. Cook. Measurement of ozone and water vapor by airbus in-service aircraft: The mozaic airborne program, an overview. *J. Geophys. Res.*, 103:25631–25642, 1998.
- [49] R. S. Märkl, C. Voigt, D. Sauer, R. K. Dischl, S. Kaufmann, T. Harlaß, V. Hahn, A. Roiger, C. Weiß-Rehm, U. Burkhardt, U. Schumann, A. Marsing, M. Scheibe, A. Dörnbrack, C. Renard, M. Gauthier, P. Swann, P. Madden, D. Luff, R. Sallinen, T. Schripp, and P. Le Clercq. Powering aircraft with 100 % sustainable aviation fuel reduces ice crystals in contrails. *Atmospheric Chemistry and Physics*, 24(6):3813–3837, 2024. doi: 10.5194/acp-24-3813-2024. URL <https://acp.copernicus.org/articles/24/3813/2024/>.
- [50] Valérie Masson-Delmotte, Panmao Zhai, Hans-Otto Pörtner, Debra Roberts, Jim Skea, Priyadarshi R Shukla, et al. *Global Warming of 1.5 C: IPCC special report on impacts of global warming of 1.5 C above pre-industrial levels in context of strengthening response to climate change, sustainable development, and efforts to eradicate poverty*. Cambridge University Press, 2022.
- [51] Ralf Meerkötter, U Schumann, DR Doelling, P Minnis, T Nakajima, and Y Tsushima. Radiative forcing by contrails. In *Annales Geophysicae*, volume 17, pages 1080–1094. Springer, 1999.

- [52] Daniel M Murphy and Thomas Koop. Review of the vapour pressures of ice and supercooled water for atmospheric applications. *Quarterly Journal of the Royal Meteorological Society: A journal of the atmospheric sciences, applied meteorology and physical oceanography*, 131(608):1539–1565, 2005.
- [53] G. Myhre and F. Stordal. On the tradeoff of the solar and thermal infrared radiative impact of contrails. *Geophys. Res. Lett.*, 28:3119–3122, 2001.
- [54] Frank Noppel and Riti Singh. Overview on contrail and cirrus cloud avoidance technology. *Journal of Aircraft*, 44(5):1721–1726, 2007.
- [55] J. Pletzer and V. Grewe. Sensitivities of atmospheric composition and climate to altitude and latitude of hypersonic aircraft emissions. *Atmospheric Chemistry and Physics*, 24(3):1743–1775, 2024. doi: 10.5194/acp-24-1743-2024. URL <https://acp.copernicus.org/articles/24/1743/2024/>.
- [56] Regina Pouzolz, Oliver Schmitz, and Hermann Klingels. Evaluation of the climate impact reduction potential of the water-enhanced turbofan (wet) concept. *Aerospace*, 8(3), 2021. ISSN 2226-4310. doi: 10.3390/aerospace8030059. URL <https://www.mdpi.com/2226-4310/8/3/59>.
- [57] G. Rädcl and K. Shine. Evaluation of the use of radiosonde humidity data to predict the occurrence of persistent contrails. *Quart. J. Roy. Met. Soc.*, 133: 1413–1423, 2007.
- [58] J. Rosenow and H. Fricke. Individual condensation trails in aircraft trajectory optimization. *Sustainability*, 11:6082, 2019. doi: 10.3390/su11216082.
- [59] Jorge L. Sarmiento and Nicolas Gruber. *Ocean Biogeochemical Dynamics*. Princeton University Press, Princeton, 2006. ISBN 9781400849079. doi: doi: 10.1515/9781400849079. URL <https://doi.org/10.1515/9781400849079>.
- [60] R. Sausen, K. Gierens, M. Ponater, and U. Schumann. A diagnostic study of the global distribution of contrails, part i. present day climate. *Theor. Appl. Climatol.*, 61:127–141, 1998.
- [61] Robert Sausen, Sina Maria Hofer, Klaus Martin Gierens, Luca Bugliaro Goggia, Rüdiger Ehrmanntraut, Ilona Sitova, Kacper Walczak, Anja Burrige-Diesing, Milena Bowman, and Nick Miller. Can we successfully avoid persistent contrails by small altitude adjustments of flights in the real world? *Meteorologische Zeitschrift*, 2023. URL <https://api.semanticscholar.org/CorpusID:260037764>.

- [62] Ernst Schmidt. Die Entstehung von Eisnebel aus den Auspuffgasen von Flugmotoren, 1941. URL <https://elib.dlr.de/107948/>. Eintrag von Ulrich Schumann, zur Sicherstellung des Zugangs zu diesem wissenschaftshistorisch wichtigen Dokument; mit Zustimmung des Rechteinhabers (Nachfolger des Oldenbourg Verlags).
- [63] Oliver Schmitz, Hermann Klingels, and Petra Kufner. Aero Engine Concepts Beyond 2030: Part 1—The Steam Injecting and Recovering Aero Engine. *Journal of Engineering for Gas Turbines and Power*, 143(2):021001, 01 2021. ISSN 0742-4795. doi: 10.1115/1.4048985. URL <https://doi.org/10.1115/1.4048985>.
- [64] Ulrich Schumann. On conditions for contrail formation from aircraft exhausts. *Meteorologische Zeitschrift*, 5:4–23, 1996.
- [65] Ulrich Schumann. Influence of propulsion efficiency on contrail formation. *Aerospace Science and Technology*, 4(6):391–401, 2000. ISSN 1270-9638. doi: [https://doi.org/10.1016/S1270-9638\(00\)01062-2](https://doi.org/10.1016/S1270-9638(00)01062-2). URL <https://www.sciencedirect.com/science/article/pii/S1270963800010622>.
- [66] Ulrich Schumann. A contrail cirrus prediction model. *Geoscientific Model Development*, 5(3):543–580, 2012.
- [67] A. Seifert, A. Khain, A. Pokrovsky, and K.D. Beheng. A comparison of spectral bin and two-moment bulk mixed-phase cloud microphysics. *Atmospheric Research*, 80:46–66, 2006.
- [68] A Seifert, C Köhler, and KD Beheng. Aerosol-cloud-precipitation effects over germany as simulated by a convective-scale numerical weather prediction model. *Atmospheric Chemistry and Physics*, 12(2):709–725, 2012.
- [69] Surjit Singh. Method of suppressing of contrails and and solution therefor, April 1991. Patent US 5005-355-A.
- [70] D Sonntag. Advancements in the field of hygrometry. *Meteorologische Zeitschrift*, 3(2), Jan 1994. doi: 10.1127/metz/3/1994/51.
- [71] P. Spichtinger, K. Gierens, U. Leiterer, and H. Dier. Ice supersaturation in the tropopause region over lindenbergl, germany. *Meteorol. Z.*, 12:143–156, 2003.
- [72] P. Spichtinger, K. Gierens, and A. Dörnbrack. Formation of ice supersaturation by mesoscale gravity waves. *ACP*, 5:1243–1255, 2005.

- [73] P. Spichtinger, K. Gierens, and H. Wernli. A case study on the formation and evolution of ice supersaturation in the vicinity of a warm conveyor belt's outflow region. *ACP*, 5:973–987, 2005.
- [74] N. Stuber, P. Forster, G. Rädcl, and K. Shine. The importance of the diurnal and annual cycle of air traffic for contrail radiative forcing. *Nature*, 441:864–867, 2006.
- [75] Ralf Sussmann and Klaus M. Gierens. Lidar and numerical studies on the different evolution of vortex pair and secondary wake in young contrails. *Journal of Geophysical Research: Atmospheres*, 104(D2):2131–2142, 1999. doi: <https://doi.org/10.1029/1998JD200034>. URL <https://agupubs.onlinelibrary.wiley.com/doi/abs/10.1029/1998JD200034>.
- [76] R. Teoh, U. Schumann, E. Gryspeerdt, M. Shapiro, J. Molloy, G. Koudis, C. Voigt, and M.E.J. Stettler. Aviation contrail climate effects in the north atlantic from 2016 to 2021. *Atmos. Chem. Phys.*, 22:10919—10935, 2022. doi: 10.5194/acp-22-10919-2022.
- [77] R. Teoh, Z. Engberg, U. Schumann, C. Voigt, M. Shapiro, Susanne Rohs, and M.E.J. Stettler. Global aviation contrail climate effects from 2019 to 2021. *Atmos. Chem. Phys.*, 24:6071–6093, 2024. doi: 10.5194//acp-24-6071-2024.
- [78] Roger Teoh, Ulrich Schumann, and Marc E. J. Stettler. Beyond contrail avoidance: Efficacy of flight altitude changes to minimise contrail climate forcing. *Aerospace*, 7(9), 2020. ISSN 2226-4310. doi: 10.3390/aerospace7090121. URL <https://www.mdpi.com/2226-4310/7/9/121>.
- [79] Otto Tetens. Über einige meteorologische Begriffe. *Z. geophys.*, 6:297–309, 1930.
- [80] David N Thomas. *Sea ice*. John Wiley & Sons, 2017.
- [81] R. Treffeisen, R. Krejci, J. Ström, A.C. Engvall, A. Herber, and L. Thomason. Humidity observations in the arctic troposphere over ny-alesund, svalbard based on 15 years of radiosonde data. *Atmos. Chem. Phys.*, 7:2721–2732, 2007.
- [82] Florian Ungeheuer, Lucía Caudillo, Florian Ditas, Mario Simon, Dominik van Pinxteren, Doğuşhan Kılıç, Diana Rose, Stefan Jacobi, Andreas Kürten, Joachim Curtius, et al. Nucleation of jet engine oil vapours is a large source of aviation-related ultrafine particles. *Communications Earth & Environment*, 3(1):319, 2022.

- [83] Nadine Unger, Tami C. Bond, James S. Wang, Dorothy M. Koch, Surabi Menon, Drew T. Shindell, and Susanne Bauer. Attribution of climate forcing to economic sectors. *Proceedings of the National Academy of Sciences*, 107(8):3382–3387, 2010. doi: 10.1073/pnas.0906548107. URL <https://www.pnas.org/doi/abs/10.1073/pnas.0906548107>.
- [84] S. Unterstrasser. Properties of young contrails – a parametrisation based on large-eddy simulations. *Atmospheric Chemistry and Physics*, 16(4):2059–2082, 2016. doi: 10.5194/acp-16-2059-2016. URL <https://acp.copernicus.org/articles/16/2059/2016/>.
- [85] S. Unterstrasser and N. GörSCH. Aircraft-type dependency of contrail evolution. *Journal of Geophysical Research: Atmospheres*, 119(24):14,015–14,027, 2014. doi: <https://doi.org/10.1002/2014JD022642>. URL <https://agupubs.onlinelibrary.wiley.com/doi/abs/10.1002/2014JD022642>.
- [86] Simon Unterstrasser. The contrail mitigation potential of aircraft formation flight derived from high-resolution simulations. *Aerospace*, 7(12), 2020. ISSN 2226-4310. doi: 10.3390/aerospace7120170. URL <https://www.mdpi.com/2226-4310/7/12/170>.
- [87] Christiane Voigt, Jonas Kleine, Daniel Sauer, Richard H Moore, Tiziana Bräuer, Patrick Le Clercq, Stefan Kaufmann, Monika Scheibe, Tina Jurkat-Witschas, Manfred Aigner, et al. Cleaner burning aviation fuels can reduce contrail cloudiness. *Communications Earth & Environment*, 2(1):114, 2021.
- [88] Georg von Bonhorst, Moritz Maizet, and Klaus Gierens. On contrail prediction under realistic weather forecast uncertainty. *Meteorol. Z.*, 2024. submitted.
- [89] Eugene Wagner, David Jacques, William Blake, and Meir Pachter. Flight test results of close formation flight for fuel savings. In *AIAA Atmospheric Flight Mechanics Conference and Exhibit*, page 4490, 2002.
- [90] Lena Wilhelm, Klaus Gierens, and Susanne Rohs. Weather variability induced uncertainty of contrail radiative forcing. *Aerospace*, 8(11), 2021. ISSN 2226-4310. doi: 10.3390/aerospace8110332. URL <https://www.mdpi.com/2226-4310/8/11/332>.
- [91] K. Wolf, N. Bellouin, and O. Boucher. Radiative effect by cirrus cloud and contrails – a comprehensive sensitivity study. *EGUsphere*, Preprint:1–38, 2023. doi: 10.5194/egusphere-2023-155.
- [92] F. Yin, V. Grewe, and K. Gierens. Impact of hybrid electric aircraft on contrail coverage. *Aerospace*, 7:147, 2020. doi: 10.3390/aerospace7100147.

- [93] F. Yin, V. Grewe, F. Castino, P. Rao, S. Matthes, K. Dahlmann, S. Dietmüller, C. Frömming, H. Yamashita, P. Peter, E. Klingaman, K. Shine, B. Lührs, and F. Linke. Predicting the climate impact of aviation for en-route emissions: The algorithmic climate change function submodel accf 1.0 of emac 2.53. *Geosci. Model. Dev. Discuss.*, 16:3313–3334, 2023. doi: 10.5194/gmd-16-3313-2023.
- [94] Richard E. Zeebe. History of seawater carbonate chemistry, atmospheric co₂, and ocean acidification. *Annual Review of Earth and Planetary Sciences*, 40 (Volume 40, 2012):141–165, 2012. ISSN 1545-4495. doi: <https://doi.org/10.1146/annurev-earth-042711-105521>. URL <https://www.annualreviews.org/content/journals/10.1146/annurev-earth-042711-105521>.

Acknowledgements

I would like to express my gratitude to everyone who supported me throughout my research and writing journey, particularly:

- My supervisor Klaus, who introduced me to the subject area and supported me in numerous aspects, such suggesting literature, answering scientific questions or giving helpful suggestions and hints. Collaborating with you and generating fresh ideas was truly enjoyable. I was able to learn a lot from you and your years of experience. Thank you!
- Robert Sausen from whom I learnt about this topic for the first time. He arranged my thesis with Klaus.
- Luca Bugliaro my second supervisor, who taught me a lot about how satellites work and the contrail detection algorithm.
- Anja Schmidt for reviewing my thesis and helping me with the organisational issues regarding the university.
- Moritz Maizet, the third author of the paper. It was a pleasure working with you during your internship.
- The D-KULT project (Demonstrator Klimafreundliche Luftfahrt413 (Förderkennzeichen 20M2111A), within the Luftfahrtforschungsprogramm LuFo VI), in the course of which this work was created here, and the DKRZ (Deutsches Klimarechenzentrum) for the funds and resources that enabled this research.
- Ulrike Burkhardt for the idea to compare the cloudiness in the different regions and Markus Rapp as well as Luca Bugliaro for reviewing a draft version of the paper and giving valuable feedback.
- Anja Blum, Sina Hofer and Dario Sperber for helping with organisational issues.

- To my colleagues at the institute and project with whom I had many interesting conversations. I would especially like to thank the PhDs in the "Rechenzentrum" for making me feel welcome and helping me settle in.
- My family who always supported me in my studies.

Without you and many others, this work would not have been possible.

Selbständigkeitserklärung

Hiermit erkläre ich, die vorliegende Arbeit mit dem Titel

**Stability assessment of forecasts regarding ice supersaturation and
persistent contrails**

selbständig verfasst zu haben und keine anderen als die in der Arbeit angegebenen
Quellen und Hilfsmittel benutzt zu haben.

München, den 15.10.2024

Georg von Bonhorst